Nanoscale

MINIREVIEW

View Article Online
View Journal | View Issue

Cite this: *Nanoscale*, 2021, **13**, 5620

Synthesis and defect engineering of molybdenum oxides and their SERS applications

Chenjie Gu, *†[a] Delong Li, †[b] Shuwen Zeng, *[c] Tao Jiang, [a] Xiang Shen [a] and Han Zhang *[b]

Surface-enhanced Raman scattering (SERS) spectroscopy has been developed into a cross-disciplinary analytical technology through exploring various materials' Raman vibrational modes with ultra-high sensitivity and specificity. Although conventional noble-metal based SERS substrates have achieved great success, oxide-semiconductor-based SERS substrates are attracting researchers' intensive interest due to their merits of facile fabrication, high uniformity and tunable SERS characteristics. Among all the SERS active oxide semiconductors, molybdenum oxides (MoO_x) possess exceptional advantages of high Raman enhancement factor, environmental stability, recyclable detection, *etc*. More interestingly, the SERS effect of the MoO_x SERS substrates may involve both the electromagnetic enhancement mechanism and the chemical enhancement mechanism, which is determined by the stoichiometry and morphology of the material. Therefore, the focus of this review will be on two critical points: (1) synthesis and material engineering methods of the functional MoO_x material and (2) MoO_x SERS mechanism and performance evaluation. First, we review recent works on the MoO_x preparation and material property tuning approaches. Second, the SERS mechanism and performance of various MoO_x substrates are surveyed. In particular, the performance uniformity, enhancement factor and recyclability are evaluated. In the end, we discuss several challenges and open questions related to further promoting the MoO_x as the SERS substrate for monitoring extremely low trace molecules and the theory for better understanding of the SERS enhancement mechanism.

Received 30th October 2020,
Accepted 9th February 2021

DOI: 10.1039/d0nr07779h

rsc.li/nanoscale

Introduction

The enhanced Raman scattering phenomenon was first reported by M. Fleischmann on a roughened silver electrode coated with pyridine in 1974.[1] Hereafter, research works conducted by Jeanmaire and Van Duyne, Albrecht and Creighton further laid solid foundations for this Raman enhancement phenomenon, which was named surface-enhanced Raman scattering (SERS).[2,3] Today, the SERS technique has become a cross-disciplinary analytical tool endorsed by the merits of non-destructivity, ultra-high sensitivity and specificity, and the great achievements of the SERS technique are expediting its application in the fields of chemical engineering, biological sensing, food safety, environmental protection, *etc*.[4–17]

Conventionally, SERS detection relies on the surface electromagnetic field or "hot spots", which are produced by the surface plasmon polaritons that are excited by the incident Raman laser on the noble metal surface (Au, Ag, Cu, *etc*.) with the different nanostructures, and normally up to 7–8 orders of molecules' Raman scattering signal enhancement could be obtained.[18–23] Experimentally, for the purpose of strengthening the surface electromagnetic field induced by the surface plasmon polaritons and consequently promoting the electromagnetic enhancement mechanism (EM), researchers have made great effort for designing and preparing novel noble metal nanostructures or compounds, and substantial improvement in the SERS performance has been achieved.[24–27] However, meticulous control of the nanostructures to produce strong surface plasmon polaritons is not an easy task. Besides, with a continuous expansion of challenging applications, noble metals usually show poor stability, biocompatibility and large-scale uniformity, which further impedes their practical application a lot.[28–30]

In the meantime, oxide semiconductors have been extensively studied for their superior light-material interaction capa-

[a]*Institute of Photonics, Ningbo University, 818 Feng Hua Road 315211, Ningbo, China. E-mail: guchenjie@nbu.edu.cn*
[b]*Collaborative Innovation Center for Optoelectronic Science & Technology, International Collaborative Laboratory of 2D Materials for Optoelectronics Science and Technology of Ministry of Education, Institute of Microscale Optoelectronics, Shenzhen University, Shenzhen 518060, China. E-mail: hzhang@szu.edu.cn*
[c]*XLIM Research Institute, UMR 7252, CNRS/University of Limoges, Avenue Albert Thomas, 87060 Limoges, France. E-mail: shuwen.zeng@unilim.fr*
† These authors contributed equally to this work.

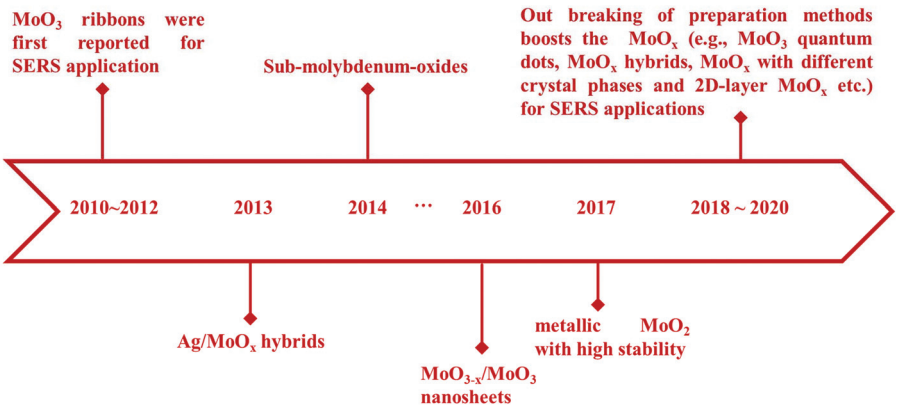

Fig. 1 A concise timeline depicting the emergence of MoO_x nanostructures for SERS application.

bilities, and numerous application cases by manipulating the light-material interaction modes or strength have been demonstrated in the early literature;[31–34] however, the SERS phenomenon on the oxide semiconductors, as one of the important light-material interaction cases, initially has received much less attention in comparison with that on noble metals due to the weak Raman signal enhancement capability.[35] Until recently, the outbreak of synthesis methods for preparing oxide semiconductors with various chemical stoichiometries and morphologies has promoted the intensive research of oxide semiconductors for SERS application.[36,37] Experimental results show that materials such as titanium oxides (TiO_{2-x}), cuprous oxides (Cu_2O), zinc oxides (ZnO_x), reduced graphene oxides (rGO), tungsten oxides (WO_{3-x}), molybdenum oxides (MoO_x), *etc*. show promising SERS characteristics. In the meantime, SERS mechanism investigation on these materials also reveals that either the electromagnetic enhancement/chemical enhancement or both of them exist, which brings extra advantages for the oxide semiconductors as SERS substrates.[38–47] Impressively, among all these oxide semiconductors, MoO_x show exceptional SERS characteristics, which is ascribed to the diverse defect engineering approaches and widely tunable free electron concentrations; therefore plentiful research works have been reported in recent years.[36,48]

Molybdenum oxides are a kind of versatile transition metal oxide with various applications in the fields of chemical catalysts, bio-sensing, energy storage, fluorescence detection, electrochromic glass, hole transport layers, *etc*. For example, Cheng *et al.* reported the use of Pd/MoO_{3-x} hybrids as a chemical catalyst for ammonia borane hydrolysis. Xiao *et al.* implemented the MoO_x quantum dots to probe the 2,4,6-trinitrotoluene, while Balendhran *et al.* fabricated a field effect transistor by using the MoO_3 as the channel material for bovine serum albumin (BSA) detection. And Achadu *et al.* used antibody modified magnetic-derivatized plasmonic molybdenum trioxide quantum dots as the plasmonic/magnetic agent, and the antibody modified fluorescent graphitic carbon nitride quantum dots as the monitoring probe for virus detection.[49–55] Experimentally, MoO_x have several different crystal structures, and the relatively stable one is the orthorhombic structure (α-MoO_3), whereas the monoclinic structure (β-MoO_3), MoO_3-II (ε-MoO_3) and hexagonal structure (h-MoO_3) are metastable phases. Moreover, MoO_x also show rich variants on morphologies and chemical stoichiometries. Therefore, in order to achieve MoO_x with diverse functions, tremendous efforts have been made to explore advanced material preparation and engineering strategies. Generally, methods of chemical liquid synthesis and vapour deposition are extensively reported, *e.g.*, sputtering, evaporation, chemical vapour deposition, physical vapour deposition, *etc*.

To date, a great number of studies on MoO_x for SERS applications have been reported since the first use of MoO_x ribbons as SERS substrates in 2010.[56] Especially in the recent three years, various functional MoO_x materials have been prepared and remarkable SERS performance improvement has been achieved (Fig. 1); however a thorough review of MoO_x material preparation, defect engineering methods, and SERS mechanism discussions and performance evaluations are still lacking. Herein, in this minireview, we will emphasize the SERS application of the MoO_x. First, we briefly introduce the fundamental material properties, *e.g.*, crystalline structures and band structure of MoO_x. Then, we mainly focus on the diverse preparation methods and material engineering strategies for altering the physical and chemical properties of MoO_x. Next, we discuss the SERS mechanism as well as the SERS performance of MoO_x and MoO_x hybrids. Finally, we summarize the papers, several challenges and open questions of MoO_x as the promising SERS substrates for monitoring extremely low trace molecules as well as the theory for better understanding the SERS enhancement mechanism.

Fundamental material properties and synthesis methods

Crystal structures

Molybdenum oxides have several crystal structures, namely α-MoO_3, β-MoO_3, ε-MoO_3 and h-MoO_3. Experimental evidence

indicates that α-MoO_3 is thermally stable, whereas β-MoO_3, ε-MoO_3 and h-MoO_3 are metastable phases, and phase transformation from the metastable phase of β-MoO_3 and h-MoO_3 to α-MoO_3 is ready to happen under high temperature conditions.

α-MoO_3 has an orthorhombic structure with cell parameters of a = 3.962 Å, b = 13.85 Å and c = 3.697 Å (Fig. 1a), respectively.[57,58] α-MoO_3 possesses a typical layered crystal structure, which is constructed by the linked and distorted MoO_6 octahedra sharing four corners to form double layers. More specifically, the MoO_6 octahedra forms edge-sharing along the [001] crystal direction and corner sharing rows along the [100] crystal direction in the double-layer sheet, and the double-layer sheet stacks are maintained by the weak van der Waals (vdW) forces along the [010] crystal direction. The thickness of the double layers constructed by the distorted MoO_6 octahedra is about 14 Å, whereas the vdW gaps between the neighbouring layers are 6.9 Å.[59] The above layered crystal structure provides the possibility of creating two dimensional (2D) α-MoO_3 sheets.[60] Moreover, it can be observed in the octahedron that the oxygen atoms can be categorized into three types based on their coordination number (inset of Fig. 2a), which is terminal oxygen (O_t), asymmetric oxygen (O_a), and symmetrically bridging oxygen (O_s). The O_t bonds to single Mo and the bond length is 1.67 Å. However the O_a laterally bonds to two Mo atoms and the bond lengths are 1.74 Å and 2.25 Å, respectively. The O_s bonds to three Mo atoms, the length of two horizontal bonds is 1.95 Å, and the vertical one is 2.33 Å. Charge distribution analysis of the Mo–O bonds in the MoO_6 octahedron reveals a strong covalent characteristic on the shortest Mo–O bond, whereas ionic bonds dominate the longest Mo–O bond.[61,62]

β-MoO_3 has a monoclinic structure, the cell parameters of the β-MoO_3 crystal phase are a = 5.6109 Å, b = 4.8562 Å and c = 5.6285 Å, while the monoclinic angle is 120.95° (Fig. 2b). The structure of β-MoO_3 is a kind of monoclinically distorted variant of ReO_3, in which the MoO_6 octahedra share the corner and form distorted strings in the [001] crystal direction.[63] In the meantime, the Mo atom corners within the strings are pairwise drawn nearer to each other to form doublets, resulting in the distortion of the MoO_6 octahedra and elimination of the crystal plane. Moreover, in the string of the MoO_6 octahedra, the distorted angle is 13.18°, and the Mo atom lies within the octahedra, bonding to six inequivalent O atoms with a bond length of 1.694, 2.054, 1.766, 2.288, 1.800 and 2.056 Å, respectively. Finally, as a metastable phase, it is reported that β-MoO_3 will transform into the α-phase by heating above 673 K.[64]

The ε-MoO_3 and h-MoO_3 crystal structures are less studied than the above two. ε-MoO_3 is a high-pressure modification crystal structure, and it is with a specific monoclinic phase (Fig. 2c).[65] However h-MoO_3 has a hexagonal structure with the cell parameters determined to be a = b = 10.57 Å and c = 3.725 Å (Fig. 2d).[66] The structure of h-MoO_3 is constructed with the MoO_6 octahedra by chaining them in zigzag. Moreover, the unique feature of the h-MoO_3 is that the octahedra chains build a hexagonal crystalline structure, and create large one-dimensional tunnels along the [001] crystal direction with a diameter of ~3.0 Å.[67]

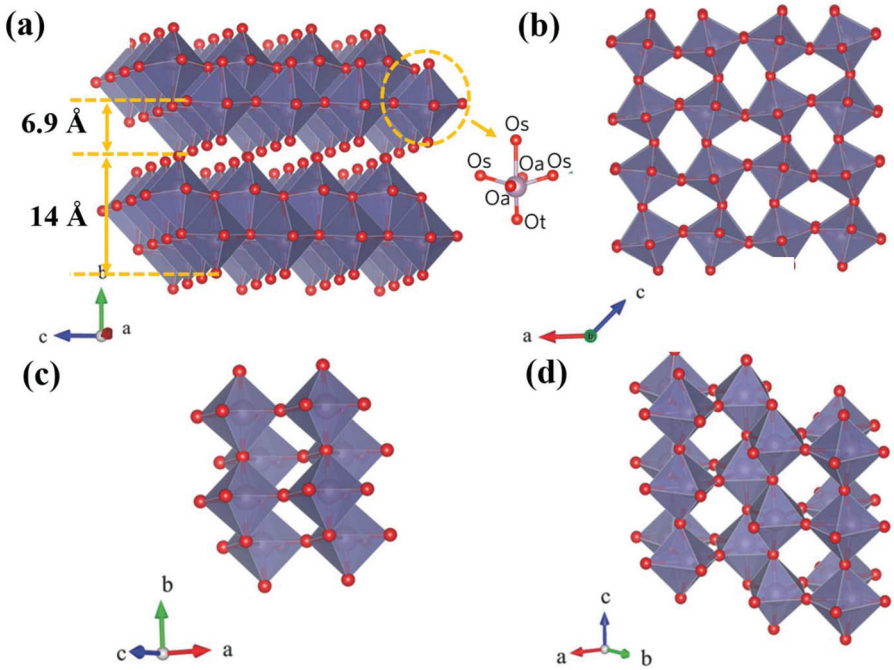

Fig. 2 (a) α-MoO_3 with an orthorhombic crystal structure. (b) β-MoO_3 with a monoclinic crystal structure. (c) ε-MoO_3 with a monoclinic crystal structure. (d) h-MoO_3 with a hexagonal crystal structure.[48] Reproduced with permission. Copyright 2017, Wiley-VCH. The inset in (a) shows the respective position of O_a, O_s and O_t in the MoO_6 octahedra.

Controllable synthesis of MoO_x

Material synthesis establishes the foundation of MoO_x as an attractive material for SERS application. Until now, a variety of synthetic approaches have been reported, which can be categorized into two primary strategies, *e.g.*, vapor-phase deposition and liquid-phase synthesis. Therefore, in this part, synthetic methods of MoO_x with different approaches are comprehensively discussed.

Vapor-phase deposition. Since the 1950s, vapour-phase deposition has been extensively investigated for the synthesis of bulk crystals.[68,69] In general, vapour-phase deposition methods are based on the deposition of vaporized target materials onto specific substrates and mainly includes physical vapour deposition (PVD), chemical vapour deposition (CVD), chemical vapour transport (CVT) and so on. Generally, through the vapour-phase deposition method, we are able to prepare MoO_x materials with controlled quality and structure, as well as large-scale production.[70,71]

For the PVD method, metallic Mo and its oxide are commonly chosen as the starting material and transited from the solid phase into vapour phase by evaporation or sputtering.[71] A range of techniques have been reported to synthesize MoO_x, such as sputtering, thermal and electron-beam evaporation, pulsed laser deposition, *etc*. These PVD techniques are suitable for the control growth of thin MoO_x films as revealed by TEM, AFM, SEM, XRD, XPS and Raman spectroscopy detection. However, it is also shown that each technique has its own characteristics and processing parameters, depending on the selection of PVD techniques.

Sputtering is a widely adopted PVD technique with a controllable growth rate and thickness for thin film deposition. In a typical sputtering process, the incident inert gas is firstly ionized to generate energetic plasma by applying a high voltage, and the ions then bombard the target source to generate sputtered flux, which will finally deposit onto the substrate to form the film product.[69] In order to prepare the MoO_x by the sputtering method, a Mo target was usually used to deposit the Mo thin film at first. Then, the MoO_x were synthesised by dry oxidation of the sputtered Mo thin film. The influence of Mo thickness variation, oxidation temperature and time on the crystallographic structure, surface morphology and roughness of the MoO_x thin films can be studied by using TEM, AFM, XRD, SEM and Raman spectroscopy. For example, Dwivedi *et al.* reported a radio-frequency (RF) sputtering method to deposit 150 and 240 nm thick Mo films at 100 W RF power under a pure argon atmosphere, and the deposited Mo films were then subjected to oxidation at 400 °C and 500 °C under O_2 ambient conditions to obtain crystal MoO_3 films.[72] Chang *et al.* studied the phases and textures of the resultant MoO_3 under different conditions. A 3 inch diameter metallic Mo target was employed as the precursor during the sputtering process. It was found that the final structure of MoO_3 was directly related to the sputtering gas composition as well as the annealing temperature. As shown in Fig. 3a, the phase variety and texture can be analysed by XRD measurement. When sputtered under a mixed Ar/O_2 atmosphere, the obtained MoO_3 films form α and/or β phase, varying with the annealing temperature. The films annealed below 350 °C show a pure β phase, films at 350–400 °C are composed of both α and β phases, and the pure α phase is obtained when the temperature is beyond 450 °C.[73]

The evaporation method (thermal and electron beam) is also a commonly used PVD technique for molybdenum oxide synthesis. The target source, usually MoO_3 powder, is melted and evaporated by heating or bombardment of high-energy electron beams, and then the vaporized source material is deposited onto the substrate to form MoO_3 with a controlled microstructure.[74,75] This technique can provide a relatively high deposition rate as well as the controllability of deposition

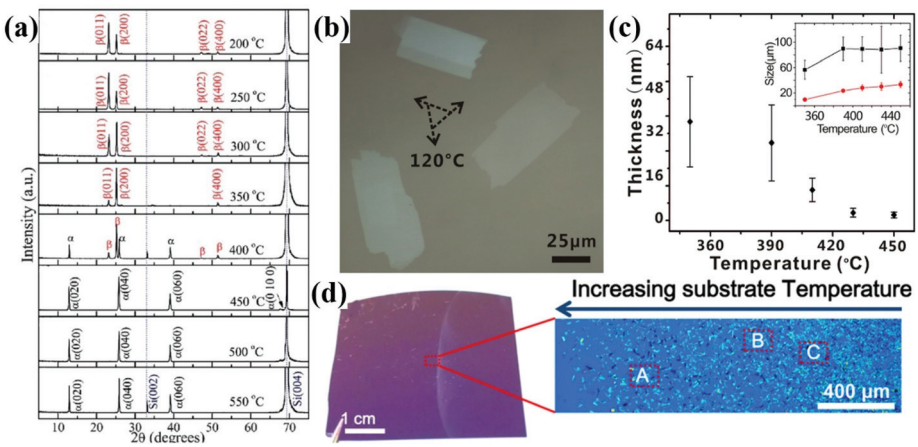

Fig. 3 (a) XRD patterns of the MoO_3 films sputtered at room temperature in 3 mTorr mixed gas and then annealed at different temperature in air for 1 h.[73] Reproduced with permission. Copyright 2011, Royal Society of Chemistry. (b) Optical micrograph of grown α-MoO_3 sheets on a mica substrate. (c) Thickness and lateral size of α-MoO_3 sheets as a function of the growth temperature.[78] Reproduced with permission. Copyright 2016, American Institute of Physics. (d) Optical image of the sample and the distribution of as-grown MoO_3.[77] Reproduced with permission. Copyright 2017, The American Chemical Society.

parameters, which enables the direct growth of thin molybdenum oxide films on various technical substrates, such as Si/SiO_2, FTO, ITO and glass substrates.[76,77] Generally, the morphologies and crystal phases of molybdenum oxide films are closely related to the sublimation and deposition temperatures. For example, Wang *et al.* reported a mica supported atomically thin α-MoO_3 crystal film by vaporized MoO_3 powder in N_2 gas, and revealed the relationship between the growth temperature and structure of as-grown MoO_3 nanosheets.[78] As shown in Fig. 3b and c, the thickness of the MoO_3 sheet is reduced and the lateral size is enlarged as the growth temperature rises. The high saturation vapor pressure and small nucleation rate of the α-MoO_3 at high temperature would result in large and ultrathin α-MoO_3 sheet growth. In a typical physical vapour deposition process, the morphology of the as prepared MoO_3 strongly depends on the substrate and source temperature, as shown in Fig. 3d. According to the optical images, the thickness of the MoO_3 nanosheets is reduced and the lateral size of the MoO_3 is enlarged when the substrate temperature increases.

Pulsed laser deposition is another efficient PVD technique, especially for electrically insulating compound targets. Different from the aforementioned sputtering or evaporation method, the vaporization energy comes from the pulsed laser, which is well suited for the semiconducting MoO_x source.[79] Camacho-López *et al.* deposited MoO_x thin films (x is between 1.8 and 2.1) and observed the structural transformation from amorphous MoO_x to mixed α and β phases of MoO_3.[80] Except for the technical parameters (including deposition temperature, substrate and oxygen gas flow rate), the laser wavelength, power density and pulse duration also have great effects on the growth process.[81] In the typical experiment, ultraviolet lasers are most commonly used for the deposition of MoO_3 films, such as argon fluoride (193 nm), krypton fluoride (248 nm), and xenon fluoride (351 nm) excimer lasers.[80,82–84]

The CVD method is an advantageous vapour-phase based direct growth process for MoO_x synthesis, which is analogous to the abovementioned PVD method. The difference is that carbonyl materials, such as molybdenum hexacarbonyl ($Mo(CO)_6$), are used as precursors during the CVD process.[85,86] Benefiting from the volatile property of precursors, CVD requires much lower growth temperature and less energy consumption for MoO_3 deposition when compared to PVD.[87,88] MoO_2 and sub-stoichiometric molybdenum oxides (MoO_{3-x}) can be grown *via* a controlled CVD process by utilizing MoO_3 powder as the precursor.[89–91] In the literature, Wu *et al.* synthesized ultrathin MoO_2 nanosheets on an inverted SiO_2/Si substrate by reducing MoO_3 powder. As shown in Fig. 4a–c, the as-grown MoO_2 nanosheets show the micron-scale lateral size and thickness of ~9 nm, as well as high crystallinity. Wang *et al.* synthesized molybdenum oxide nanomaterials by plasma-enhanced hot filament CVD with N_2 and MoO_3 precursors.[86] In this process, the carrier gas N_2 was discharged to generate plasma, which could lead to the effective reduction of MoO_3. And the experimental results in Fig. 4d and e show that the structure of the MoO_{3-x} product with different experiment conditions can be either nanoparticles or nanosheets, depending on the N_2 flow rate and growth time.

CVT is a traditional vapour–solid growth method for single crystal deposition. The CVT growth is usually conducted in a two-zone furnace under the continuous flow of carrier gas, which involves the evaporation of volatile precursors (*e.g.* $MoO_3(OH)_2$, MoO_3) in a high-temperature zone and the deposition of products in a low-temperature zone.[92] Lee *et al.* modified the CVT process and achieved the deposition of MoO_2 thin films.[93] In their experiment, the SiO_2 substrate was placed under the MoO_3 precursor, and the dual temperature zone was not required for the film deposition. By inducing H_2 as the transport agent, MoO_3 was reduced and thus formed the volatile species, $MoO_3(OH)_2$, which can be transported in the vapour phase and deposited onto the substrate to form a homogeneous thin MoO_2 film. However, the reduction of MoO_3 involved a series of complex reactions and intermediates, for example, Mo_4O_{11} is a frequently observed intermediate for the reduction of MoO_3.[94,95] On the other hand, De Melo *et al.* reported a chemically driven isothermal closed space CVT process for pure MoO_2 synthesis.[96] Different from other methods, this CVT process can produce pure MoO_2 films without any other stoichiometric MoO_x such as MoO_3/Mo_4O_{11}.

Liquid-phase synthesis. For liquid-phase synthesis of nanostructured MoO_x materials, the synthetic methods mainly include the hydrothermal/solvothermal approach, chemical precipitation, sol–gel method, and electrochemical method. In these methods, the precursor source materials are commonly the ionic salt, acid or polymer containing Mo. These liquid-phase synthesis methods show outstanding advantages in the construction of diverse morphologies and structures for MoO_x nanomaterials, as well as lower cost and higher yield than vapor-phase deposition.

The hydrothermal/solvothermal method is one of the most extensively employed approaches for nanomaterial synthesis. Hydrothermal or solvothermal synthesis of MoO_x materials relies on the controlled crystallization of molybdenum oxide seeds from the precursor in the solution environment with high temperature and pressure.[97] This synthesis method enables the good control and chemical homogeneity of the crystal structure, morphology and size by manipulating the reaction parameters. The reactant source, reaction time and temperature, concentration and species of solvent and additive/surfactant are all key parameters for the nucleation and growth of molybdenum oxides. By properly controlling the synthesis procedures, multidimensional architectures of MoO_x nanomaterials can be designed and synthesized. A variety of micro-/nanostructures including 0D quantum dots, 1D nanorods, nanowires, nanotubes, 2D nanosheets, and 3D porous structures have been synthesized by precisely controlling the synthesis process.[98–104] Fig. 4f–h show the typical TEM and SEM morphologies of molybdenum oxide nanomaterials synthesised by using the hydrothermal or solvothermal method.[105,106] Moreover, the hydrothermal synthesis allows the phase transition between metastable and stable crystal structures of molybdenum oxides. The nucleation process of

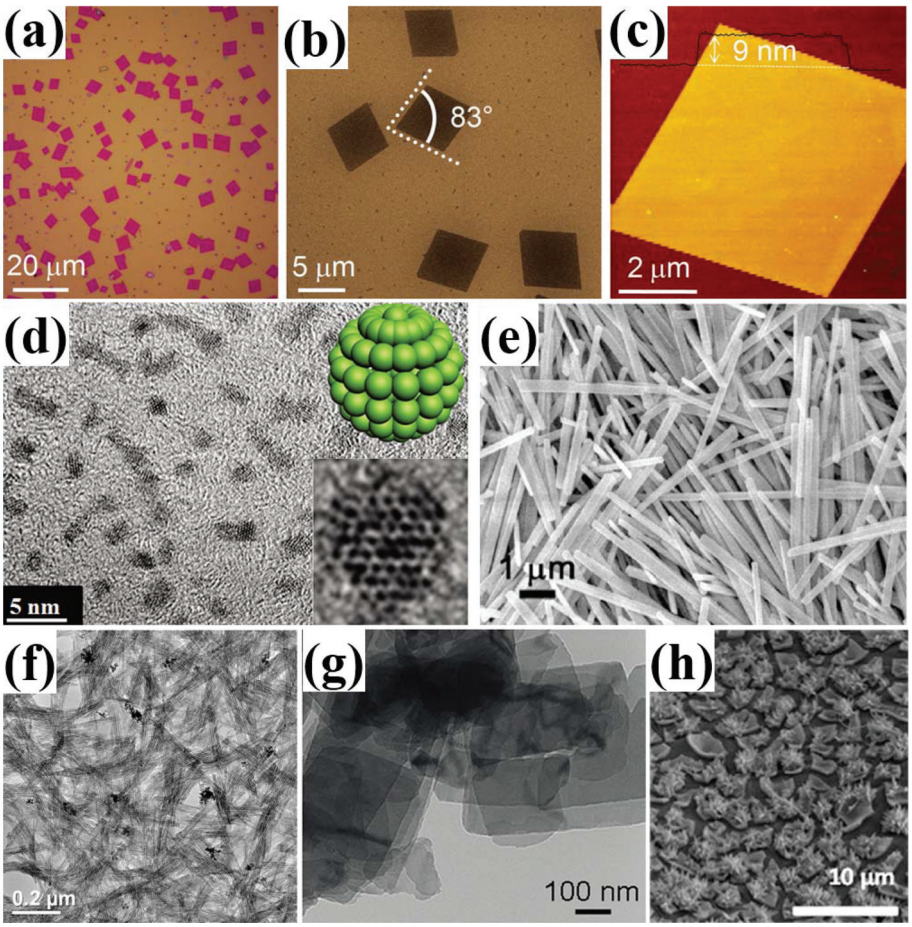

Fig. 4 (a) Optical image. (b) SEM image and (c) AFM image of MoO_2 nanosheets prepared by CVD.[89] Reproduced with permission. Copyright 2018, Wiley-VCH. (d) TEM image of MoO_{3-x} quantum dots.[98] Reproduced with permission. Copyright 2017, Royal Society of Chemistry. (e) SEM image of α-MoO_3 nanorod.[99] Reproduced with permission. Copyright 2010, The American Chemical Society. (f) TEM image of single walled MoO_3 nanotubes.[102] Reproduced with permission. Copyright 2008, The American Chemical Society. (g) TEM image of the MoO_{3-x} nanosheets.[103] Reproduced with permission. Copyright 2014, Wiley-VCH. (h) SEM image of nanoflower-like MoO_2.[106] Reproduced with permission. Copyright 2015, Royal Society of Chemistry.

different phases is found to be dependent on the concentration of acid/saline ions and temperature during the hydrothermal treatment.[107] The h-MoO_3 tends to form under the acidic aqueous environment with a high concentration of H^+, Na^+ or K^+ ions, while α-MoO_3 is more likely to be formed at a high hydrothermal temperature.[108] The hydrothermal synthesis is also an effective method to introduce oxygen vacancies or Mo ion valence tuning in the as-prepared MoO_x samples, which will be discussed in the next section.

Chemical precipitation is a facile liquid-phase synthetic method without high temperature or high pressure. Sakaushi *et al.* utilized sodium molybdenum oxide dihydrate ($Na_2MoO_4{\cdot}2H_2O$) as the precursor to synthesize nanostructured α-MoO_3, which can assemble to form a large-area freestanding film.[109] The whole process was conducted in a low-temperature (75 °C) aqueous solution with the pH of 0.5. The organic acid also exhibits strong influence on the nanostructures of α-MoO_3. In addition, Kumar *et al.* synthesized α-MoO_3 with the aid of three organic acids, citric acid (CA), tartaric acid (TA) and ethylene diamine tetra-acetic acid (EDTA).[110] The structural difference of organic ligands led to distinct morphologies of the resultant α-MoO_3 products, in which hexagonal plates were prepared in CA or TA solution, while nanorods and nanoplates were prepared in EDTA solution. Jittiarporn *et al.* carried out an intensive study on the impact of precipitation temperature on the nanostructure and physiochemical properties of MoO_3.[111] It shows that as the temperature varied from 55 to 85 °C, the crystallite size enlarged, band gap became narrower, and defects in the crystal lattice increased. At 85 °C, the h-MoO_3 crystals aggregated together and formed a flower-like cluster, which possessed a reduced band gap, increased oxygen vacancies, and best photochromic properties.

The sol–gel process is a versatile wet chemical approach for molybdenum oxide synthesis, which enables the good control of textural and morphological characteristics of materials.[112] The sol–gel method mainly undergoes several consecutive steps including: the initial hydrolysis of molecular precursors,

the following condensation and gelation, and the final drying process to obtain molybdenum oxide crystals. Tang *et al.* utilized the hydrogen peroxide treated Mo powder as the precursor to synthesize α-MoO_3 nanomaterials.[113] The obtained MoO_3 was composed of 2D nanoplates with an average size of about 1 μm and thickness of 100 nm. Morphologies of the α-MoO_3 products can be well controlled by adjusting the molar ratios of precursors, drying conditions or the additive/surfactant. Additionally, Cong *et al.* studied the influence of the relative molar ratios of molybdate and citric acid in the precursor on the growth process of α-MoO_3 samples.[114] The molar ratio of citric acid to molybdate in the precursors was demonstrated to have a significant impact on the competing crystal growth process of α-MoO_3 nanorods. The additive or surfactant can also be introduced as templates into the sol–gel process to assist the shaping of morphology and structure. For example, Brezesinski *et al.* used a poly(ethylene-*co*-butylene)-*b*-poly (ethylene oxide) block copolymer as a soft-template to synthesize a mesostructured α-MoO_3 thin film.[115] As a result, a homogeneous and porous cubic architecture MoO_3 film without obvious structural defects was successfully synthesized by this simple method. More recently, Yin *et al.* successfully synthesized well crystallized, high surface area plasmonic MoO_{3-x} by combining the evaporation induced self-assembly process and a subsequent hydrogen reduction with the assistance of F127 ($PEO_{106}PPO_{70}PEO_{106}$) as the organic template.[116] During the synthesis procedure, commercial Mo metal powder was chosen as the Mo precursor. Detailed characterization of XRD, TEM, XPS and nitrogen adsorption–desorption analysis measurement proved that the MoO_{3-x} possessed a high surface area and strong localized surface plasmon resonance under incident light.

Electrochemical methods including electrodeposition and electrochemical anodization are different kinds of economic and facile techniques for molybdenum oxide synthesis. Moreover, it is easy to proceed the structural modulation and functional modification during the electrochemical process.[117,118]

Electrodeposition is a well-suitable method for producing thin, large and uniform molybdenum oxide films. Generally, the molybdate solution, such as sodium molybdate (Na_2MoO_4), is selected as the electrolyte.[119] A further investigation demonstrated that hydrogen peroxide dissolved Mo powder can also be used for the electrodeposition of MoO_3 films.[120] More importantly, the crystallinity, phase and Mo oxidation state of the as-deposited molybdenum oxide film are reported to be very sensitive to the electrodeposition parameters. In addition, Yao *et al.* reported that the phase structure of the formation of α-MoO_3 or β-MoO_3 strongly relied on the cyclic voltammetry experimental parameters. The β-MoO_3 was formed over the potential range from −1.2 to −0.40 V (*vs.* Ag/AgCl), while α-MoO_3 was formed by applying a bias of −1.2 to 0.40 V.[57] Moreover, the bath pH is also a significant factor, which determined the oxidation state of the resultant MoO_x.[121–123]

Electrochemical anodization is another electrosynthesis method to prepare molybdenum oxide materials. By electrochemical etching and oxidation of Mo metal simultaneously, MoO_x with a controlled microstructure can be obtained. Lou *et al.* synthesized α-MoO_3 thin films by anodization of Mo foils in the ethylene glycol/water solution with sodium fluoride as the electrolyte.[124] The anodization of metallic Mo involved two competing processes, anodic oxidation and chemical dissolution. The fluoride etching of α-MoO_3 was favoured along the [001] crystal direction and crystal growth was altered and forced along [010], leading to promoted growth along (*kk*0) planes to form the platelet morphology. Szkoda *et al.* further studied the impact of fluoride ions on the morphology and porosity of synthesized films.[125] The presence of fluoride ions significantly affected the morphology of MoO_3, resulting in a maze-like architecture and the anisotropic growth along the [110] crystal direction.

Material engineering and characterization

Stoichiometric MoO_3 in the α-crystal phase is an indirect and wide band gap semiconductor with an experimentally detected band gap of ~3.1 eV, and the rest crystal phases of stoichiometric MoO_3 feature similar band gaps.[60] In recent years, density functional theory (DFT) calculations have been extensively used to investigate the MoO_x material properties. By implementing the improved calculation schemes, *e.g.*, modified Becke–Johnson potential (mBJ-GGA) method and the hybrid functional (HSE06) method, the band gap of the MoO_3 can be theoretically reproduced.[59,60] For instance, as shown in Fig. 5a, calculation of the α-MoO_3 band diagram with the mBJ-GGA method along the high symmetric points of Γ-X-S-R-T-Z-Γ in the Brillouin zone indicates that the valence band maximum (VBM) is at the R point, while the conduction band minimum (CBM) is located at the Γ point, which confirms that α-crystal MoO_3 is an indirect band gap with a band gap of about 3 eV. A similar band diagram is also obtained by using the HSE06 method. In addition, density of states (DOS) analysis in Fig. 5b–e shows that the energy band below the VBM is mainly contributed by the Mo-d and O1, 2, 3-p electron hybridization, while the contribution from Mo-s/p and O1, 2, 3-s electron states is negligible (here O1 equal to O_t, O2 equal to O_a and O3 equal to O_s). On the other hand, the energy band above the CBM is mainly contributed by the Mo-d and O1, 2, 3-p electron hybridization, and the contribution from Mo-s/p and O1, 2, 3-s electrons is insignificant.[126] At this stage, it is worth noting that experimentally prepared MoO_x usually are n-type semiconductors, which is due to the unintentional formation of intrinsic defects in the oxides (*e.g.*, oxygen vacancy); however, in order to obtain the full optical and electrical functions of MoO_x, material engineering strategies to tune the band structure, free electron concentration, morphologies, *etc.* are essentially demanded. Presently, the published literature indicates that oxygen vacancies or dopants affect the MoO_x properties a lot.[127] Other than that, structural and compound modifications such as film thickness, chemical compositions,

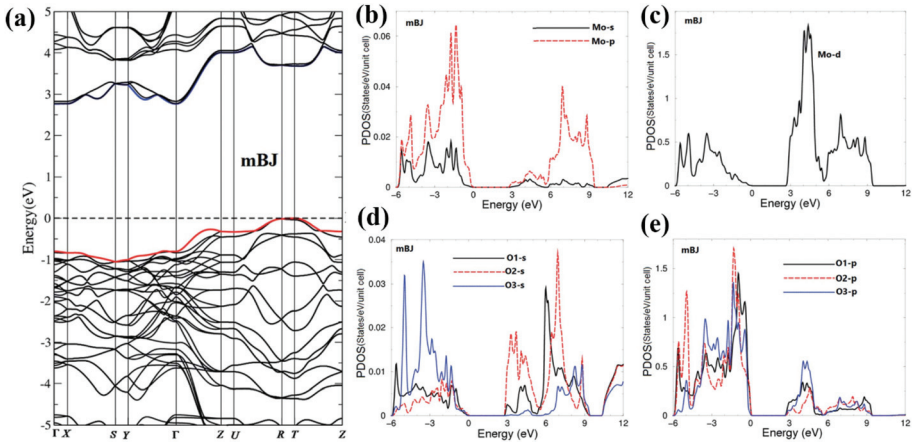

Fig. 5 (a) Band diagram calculated with the mBJ-GGA method.[60] Copyright 2015, Royal Society of Chemistry. (b) The projected DOS for the -s, -p electron of Mo. (c) The projected DOS for the -d electron of Mo. (d) The projected DOS for the -s electron of O. (e) The projected DOS for the -p electron of O. Here, O1 equal to O_t, O2 equal to O_a and O3 equal to O_s.[126] Reproduced with permission. Copyright 2017, Royal Society of Chemistry.

crystal phases and surface state control also have great influence on MoO_x properties.[128] Herein, in this section, the following strategies of tuning material properties are first reviewed: (i) oxygen vacancy creation; (ii) doping or intercalation with different types of elements; (iii) crystal phase and morphology manipulation; (iv) MoO_x hybrid formation.

Oxygen vacancy creation

As aforementioned, the orthorhombic structure of α-MoO_3 is composed of a bilayer network of MoO_6 octahedra that stacks along the [010] crystal direction, and the neighbouring bilayers bond with each other by vdW forces. The atomic structure in Fig. 2a already shows that O_t bonds to Mo, pointing perpendicular to the vdW gap in the [010] crystal direction, and O_a asymmetrically bonds to two nearby Mo ions in the [100] crystal direction, whereas O_s bonds to two Mo ions with a short bond in the [001] crystal direction and another Mo ion with a longer bond in the [010] crystal direction (Fig. 6a).[61] DFT calculations demonstrate that the formation energy of the oxygen vacancy on three different oxygen sites varies, and the

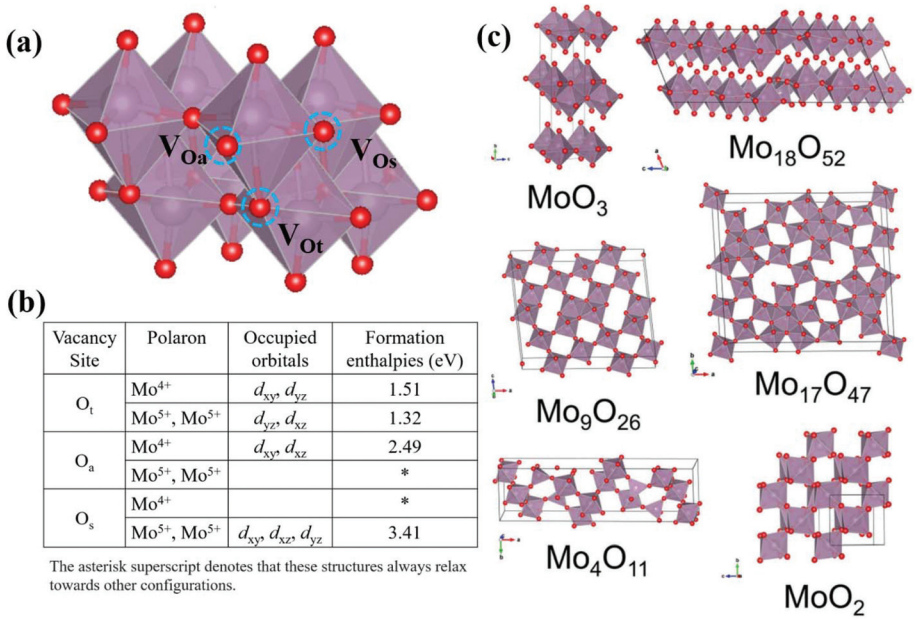

Vacancy Site	Polaron	Occupied orbitals	Formation enthalpies (eV)
O_t	Mo^{4+}	d_{xy}, d_{yz}	1.51
	Mo^{5+}, Mo^{5+}	d_{yz}, d_{xz}	1.32
O_a	Mo^{4+}	d_{xy}, d_{xz}	2.49
	Mo^{5+}, Mo^{5+}		*
O_s	Mo^{4+}		*
	Mo^{5+}, Mo^{5+}	d_{xy}, d_{xz}, d_{yz}	3.41

The asterisk superscript denotes that these structures always relax towards other configurations.

Fig. 6 (a) The possible position of forming different oxygen vacancy types in the α-MoO_3. (b) The listed formation enthalpies for the different oxygen vacancy types and polaron states in the bulk α-MoO_3. Adapted from ref. 129. Copyright 2017, The Springer Nature Publishing Group. (c) α-MoO_3 crystal structure and various defective structures with different vacancy concentrations.[126] Reproduced with permission. Copyright 2017, Royal Society of Chemistry.

lowest one is 1.32 eV, which corresponds to the oxygen vacancy formation at the O_t site (Fig. 6b). On the other hand, the formation energies of oxygen vacancies at O_a and O_s sites are 2.49 eV and 3.41 eV, which are higher than that at O_t, implying that the oxygen vacancy formation at these two respective sites is less energy favourable.[129] In the practical situation, physical characterization confirms that oxygen vacancies tend to be created at the O_t site with higher probability, and they also can be created at O_a and O_s but with lower probability, which is determined by the defect engineering strategy.[62] Besides, accounting for the number of bonded O atoms removed, a number of non-stoichiometric molybdenum-oxides with the average valence between +6 and +4 are prepared, *e.g.*, MoO_2, Mo_4O_{11}, Mo_9O_{26}, $Mo_{18}O_{52}$, Mo_4O_{11}, *etc.* (Fig. 6c).[126]

The introduction of oxygen vacancies into the MoO_3 crystal inevitably creates rich defect levels in the band gap. More insightfully, the freely vibrating electrons (two per oxygen vacancy) move close to the Mo atoms, and a portion of the wave function superimposes on the Mo–Mo (with d–d character) band, generating new energy levels lying within the band gap, while the rest is relocated to the initially empty energy levels at the edge of the conduction band (Fig. 7a).[130] Meanwhile, DOS calculation reveals more information about the defect-level positions generated by removing the O_t, O_s and O_a. It shows that the defect levels induced by the oxygen vacancies at O_a sites locate at the lower part of the band gap, and those induced by oxygen vacancies at O_t sites locate at the upper part of the band gap, whereas defect levels induced by oxygen vacancies at O_a sites are much close to the conduction band edge (Fig. 7b–d).[53] Besides, experimental evidence also shows that, for a low degree of vacancy density, the free electrons from the oxygen vacancies only occupy the bonding d–d band, and the Fermi level of the material is hardly changed. However, at a higher degree of vacancy density, more free electrons are generated, and they tend to occupy the empty d–d band in the conduction band, which consequently raises the electron filling level and shifts the Fermi level towards the conduction band.[131]

To achieve sub-molybdenum-oxides with different oxygen vacancy concentrations, effective strategies of introducing oxygen vacancies are principally important. Currently, methods of chemical reduction, semiconductor process technology, light irradiation, *etc.* are widely used. For example, sodium borohydride ($NaBH_4$), a strong inorganic reductant, can be used to react with MoO_3 nanoparticles in a mixed solution to introduce the oxygen vacancies. In the experiment, stoichiometric MoO_3 nanoflakes were first prepared by oxidizing the MoS_2 in the H_2O_2 solution, and then $NaBH_4$ was added to create the oxygen vacancies through tuning the molar ratio between the $NaBH_4$ and Mo ($NaBH_4$: Mo). It is shown in Fig. 8a that the colour of the MoO_3 suspension changes from light green, and then blue to brown with the continuous increase of reductive $NaBH_4$. The UV-vis absorption spectra in Fig. 8b also reflect an obvious peak shift, which can be ascribed to the change of free electron concentration provided by the oxygen vacancies. Furthermore, XPS detection confirms that part of the Mo^{6+} ions in MoO_3 are reduced under low

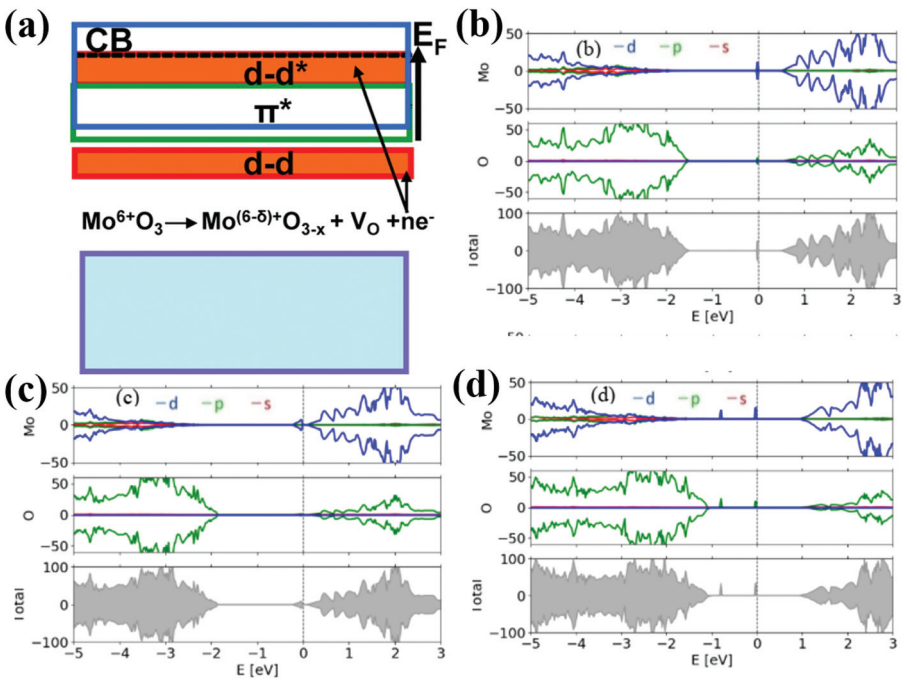

Fig. 7 (a) A schematic illustration of the electron transferring and defect level formation with the introduction of oxygen vacancies in the MoO_3.[130] Reproduced with permission. Copyright 2012, The American Chemical Society. (b) Projected DOS of the atomic supercell with V_{Os} vacancy. (c) Projected DOS of the atomic supercell with V_{Oa} vacancy. (d) Projected DOS of the atomic supercell with V_{Ot} vacancy. The blue, green and red lines represent the d, p and s orbital contributions of the corresponding atoms.[53] Reproduced with permission. Copyright 2018, EU PVSEC.

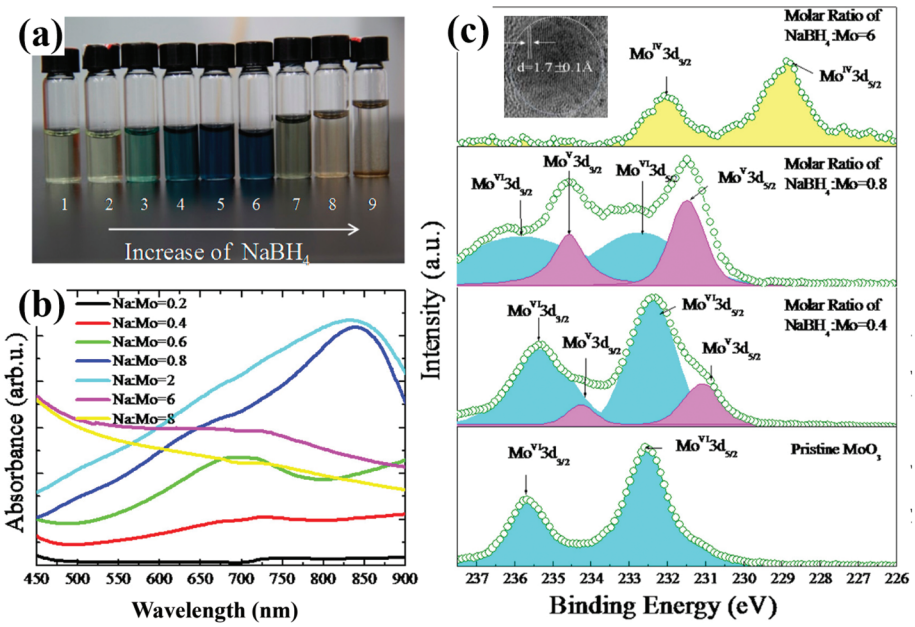

Fig. 8 (a) The color evolution of the MoO_{3-x} nanodot aqueous solution with the increase of $NaBH_4$: Mo molar ratio. (b) UV-vis absorption spectra of MoO_{3-x} nanodots prepared with different $NaBH_4$ concentrations. (c) XPS spectra of Mo 3d obtained on MoO_3 and various MoO_{3-x} nanodots prepared with different concentrations.[134] Reproduced with permission. Copyright 2017, The American Chemical Society.

molar ratio conditions; however, when the molar ratio reaches 6 : 1, all the Mo^{6+} ions are reduced to +4 valence state, and pure MoO_2 can be obtained (Fig. 8c). At this time, it also should be mentioned that, due to the layered structure of the MoO_3, EDX mapping on the reduced MoO_x indicates that Na^+ ions from $NaBH_4$ intercalate into the material, which introduce extra defect levels into the band gap.[132] Other than that, Wang *et al.* reported that, by using dopamine as the reductant, sub-molybdenum-oxides with various chemical ratios can be prepared (Fig. 9a).[133] Firstly, according to the electrochemical

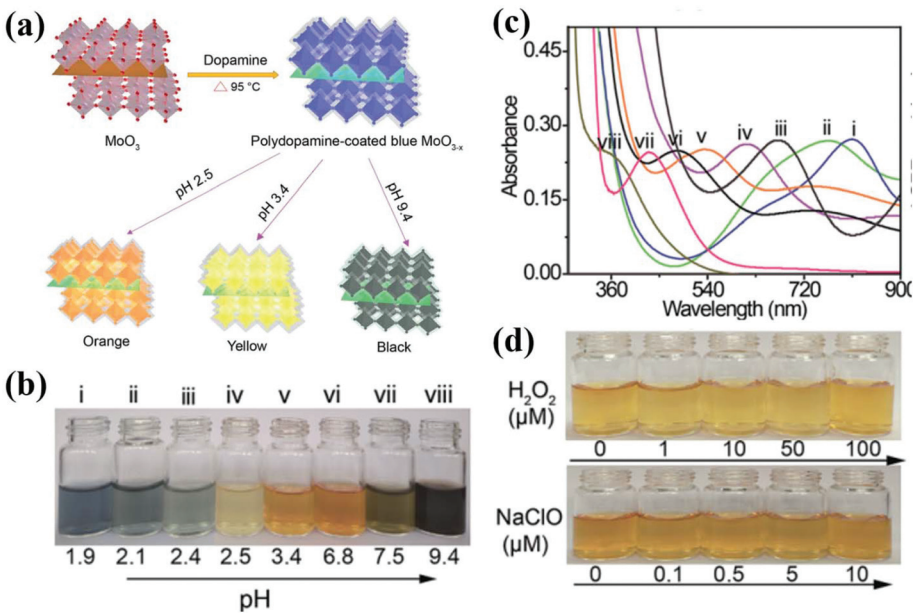

Fig. 9 (a) Schematic illustration of the preparation of PDA-coated MoO_{3-x} nanosheets with tunable plasmon resonance. (b) Photograph of the PDA-coated MoO_{3-x} nanosheets obtained under different pH values. (c) UV-Vis-NIR spectra of the MoO_{3-x} nanosheets prepared under various pH reaction solutions. (d) Photograph of yellow MoO_{3-x} nanosheets dispersed in the H_2O_2 and NaClO with different concentrations.[133] Reproduced with permission. Copyright 2019, Royal Society of Chemistry.

measurement, it reveals that the oxidation potential of dopamine decreases with the increase of the pH values. Therefore, in the experiment of MoO_3 reduction, the pH value of the MoO_3 and dopamine solution mixture was controlled, and then MoO_{3-x} nanosheets with tunable localized surface plasmon resonance (LSPR) from ultraviolet to the near-infrared region (361–809 nm) could be achieved, which also reflected on the colour change of the nanosheets that turn from deep blue, faint bluish, orange, yellow to black (Fig. 9b and c). Moreover, in Fig. 9d, it also reveals that dopamine can act as a protective surfactant, and forms polydopamine (PDA) coated MoO_x, which prevents the MoO_x from being oxidized even in the strong oxidants. Additionally, reductants such as ascorbic acid (AA), polyethylene glycol (PEG), glucose, ethanol, *etc*. also have been extensively used to tune the oxygen vacancy density, and remarkable success on tuning the oxygen vacancies has been obtained; however, using these organic reductants always introduces undesirable radicals on the material surface, which may degrade the SERS performance.[134,135]

Moreover, the electro-deposition method has plenty of advantages on preparing thin films, *e.g.*, precise control of film's stoichiometry and layer thickness, low reaction temperatures, large-scale uniformity and cost effectiveness; therefore, it also has been widely implemented for MoO_x preparation. Experimentally, through tuning the deposition parameters, *e.g.*, pulse voltage, current density, electrolyte and electrodes, the oxygen vacancy density of the deposited film can be conveniently manipulated. For instance, in the steps of electrodepositing the oxygen deficient MoO_x, a three-electrode electrodeposition system configured with Pt wire (counter electrode), ITO glass (working electrode), and Ag/AgCl (reference electrode) was used (Fig. 10a). Using the MoO_3 colloid as the electrolyte, a voltage pulse of 3 seconds and current density of 0.03 mA cm^{-2} were set as the deposition parameters. After 1200 deposition cycles, XPS detection on the deposited molybdenum oxides reveals that the MoO_{2+x} film with 61% of Mo^{6+} ion and 39% of Mo^{5+} is achieved (Fig. 10b and c).[136]

Semiconductor process technologies, such as chemical vapor deposition (CVD), magnetic sputtering, pulse laser deposition and thermal evaporation, are commonly used to tune the oxygen vacancy defects. Relying on the advantage of CVD, Wu *et al.* reported a kind of ultra-thin layer MoO_2 nanosheet prepared on the SiO_2 *via* the CVD process.[89] In the experiment, MoO_3 powder was first deposited on the SiO_2 at 750 °C for 30 minutes in the furnace by using N_2 as the carrier gas, then the sulfur (S) source was heated to 90 °C, and the evaporated S reacted with the O element in MoO_3 to create the oxygen vacancy (Fig. 11a). Raman spectra of the prepared thin film are collected. As shown in Fig. 11b, the Raman peaks at 124, 208, 230, 347, 363 and 498 cm^{-1} can be assigned to the vibration modes of MoO_2, indicating the successful deposition of the MoO_2 thin film. In the meantime, XPS detection in Fig. 11c also reveals the strong peak intensity of Mo^{4+} ions, which further confirms the formation of MoO_2.

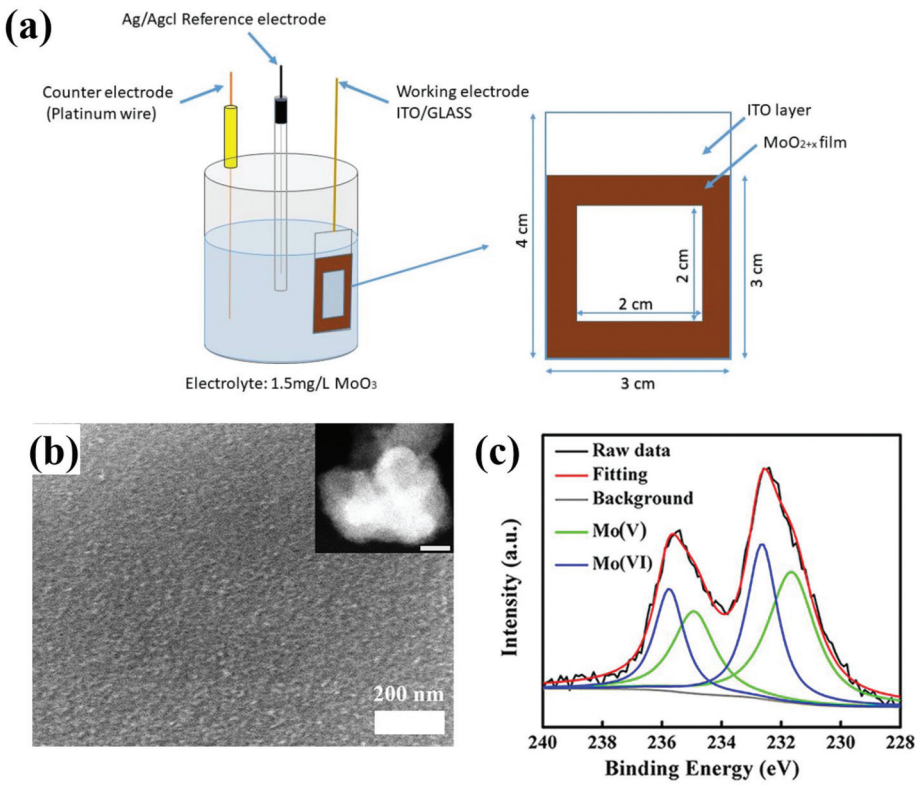

Fig. 10 (a) Schematic of MoO_{2+x} films electrodeposited on ITO glass. (b) FSEM images of the prepared MoO_{2+x} nanofilm. (c) XPS spectra of Mo 3d obtained on MoO_{2+x}.[136] Reproduced with permission. Copyright 2019, The American Chemical Society.

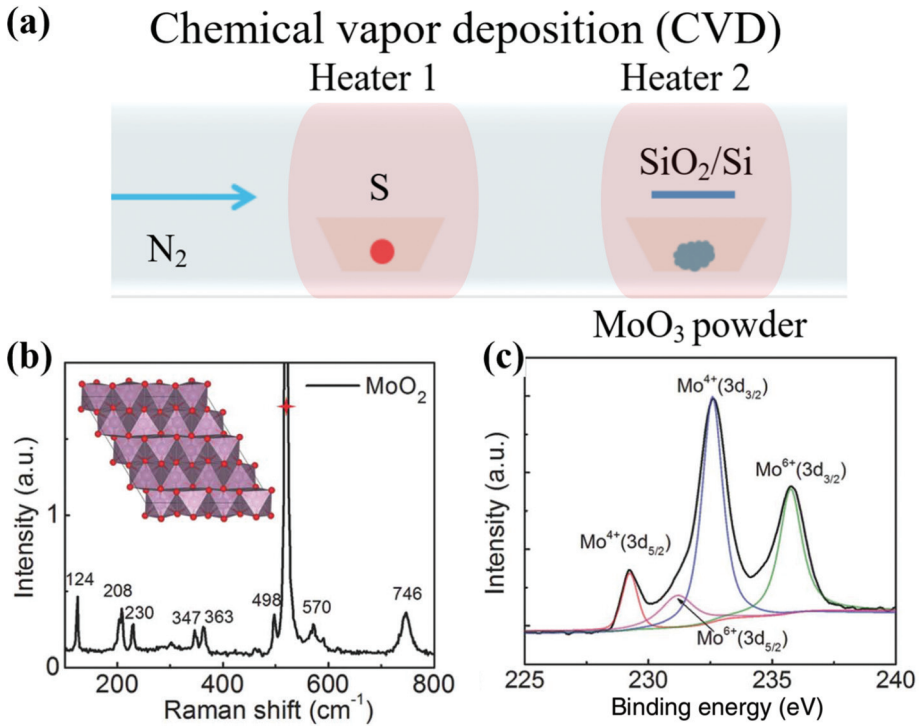

Fig. 11 (a) Schematic diagram of the CVD system. (b) Raman spectrum of MoO_2 nanosheets. (c) XPS spectrum of the Mo 3d spectrum obtained on the sample, indicating that the Mo ion in the material is mainly + 4.[89] Reproduced with permission. Copyright 2018, Wiley-VCH.

Other than that, the pulse laser deposition method is also used to shape the oxygen vacancy defect distribution in the MoO_3 through controlling the deposition temperature and oxygen partial pressure. In Khojier *et al.* research work, MoO_3 was used as the target, and different chamber temperatures and pressures were set during the process for the purpose of depositing the MoO_x film with different oxygen vacancy density.[137] XRD is performed to investigate the MoO_x film obtained under different process conditions. It is shown in Fig. 12a that the condition of 500/4.5 (500 °C, 4.5 Pa) allows the formation of orthorhombic MoO_3; however, it also shows some reflections of the Mo_4O_{11} phase, representing the for-

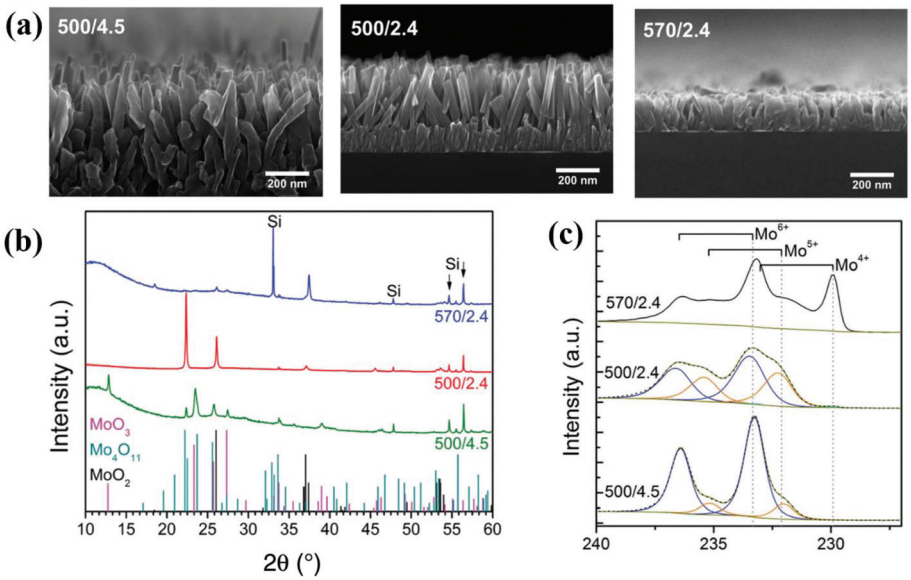

Fig. 12 (a) Molybdenum oxide deposited under different chamber conditions. (b) XRD spectra of the deposited film. (c) XPS spectra of the sample prepared under three different conditions.[126] Reproduced with permission. Copyright 2017, Royal Society of Chemistry.

mation of a mixed-phase MoO_x film. Moreover, for lower deposition pressure, the film prepared under the 500/2.4 (500 °C, 2.4 Pa) condition has reflections of Mo_4O_{11} and MoO_2, and under the process condition of 570/2.4 (570 °C, 2.4 Pa) film, it shows strong MoO_2 reflections and faint reflections of Mo_4O_{11} (Fig. 12b). The above characterization results prove the importance of the temperature as well as the O_2 partial pressure on forming the oxides with different stoichiometry. In addition, XPS detection reveals more information of the material component. It is illustrated in Fig. 12c that, for the MoO_x deposited under the 500/4.5 condition, about 13.8% of the Mo ions are Mo^{5+}, and 86.2% of the ions are Mo^{6+}. Whereas, for the MoO_x deposited at 500/2.4, Mo^{4+} ions occupy about 0.5% of the Mo ions, Mo^{5+} ions occupy another 39.4%, and the rest are Mo^{6+} ions. In the end, for the MoO_x deposited at 570/2.4, about 39.5% are Mo^{4+} ions, 31.6% of them are Mo^{5+} ions and the rest are Mo^{6+} ions. Besides, oxygen vacancies also can be created by introducing the N element into the MoO_x. In the literature, the MoO_3 film is annealed under an ammonia or N_2 atmosphere. It is demonstrated that substitution of N in the crystal introduces abundant vacancy defects into MoO_3, resulting in the enhancement of the electrical conductivity.[138,139]

Recently, light irradiation is considered as an effective strategy for creating oxygen vacancies in the oxide. A previous experiment indicates that active radicals like H^+ and OH^- can be created from H_2O in the catalytic reaction in the presence of MoO_3 under light illumination; thereafter, a substantial number of H^+ ions diffuse into the layered MoO_3, forming the OH_2 species, and then excessive OH_2 species dissociate away from the crystal, which ultimately results in the formation of oxygen vacancies (Fig. 13a and b).[95,140–142] Raman spectra are used in the experiment to monitor the evolution of 2D MoO_x suspensions under different solar light irradiation times; it is shown in Fig. 13c that, for the initial sample that is associated with α-MoO_3, Raman peaks at 280, 667, 816 and 991 cm^{-1} are observed, which is in good agreement with the vibration modes of α-MoO_3. And after 5 hours of solar light exposure, the formation of oxygen vacancies confirms that Raman peaks at 489 and 740 cm^{-1} appear, which are assigned to the stretching mode of Mo═O and Mo–O–Mo, evidencing the creation of MoO_{3-x} in the solution.

Ion doping and intercalation

Doping with extrinsic defects in the MoO_3 introduces extra energy levels in the band gap of the MoO_3 material as well. Lambert *et al.* performed DFT calculations to investigate the solubility and effect on the band structure of different metal ion doping in the MoO_3. It reveals in Fig. 14a and b that Sc, Ti and Y have limited solubility within a wide range of O_2 partial pressure at a temperature of 500 K, and thus they are restricted for efficient defect tuning. Meanwhile, Zn, Cu and Se show some solubility, especially Cu and Se appear to introduce

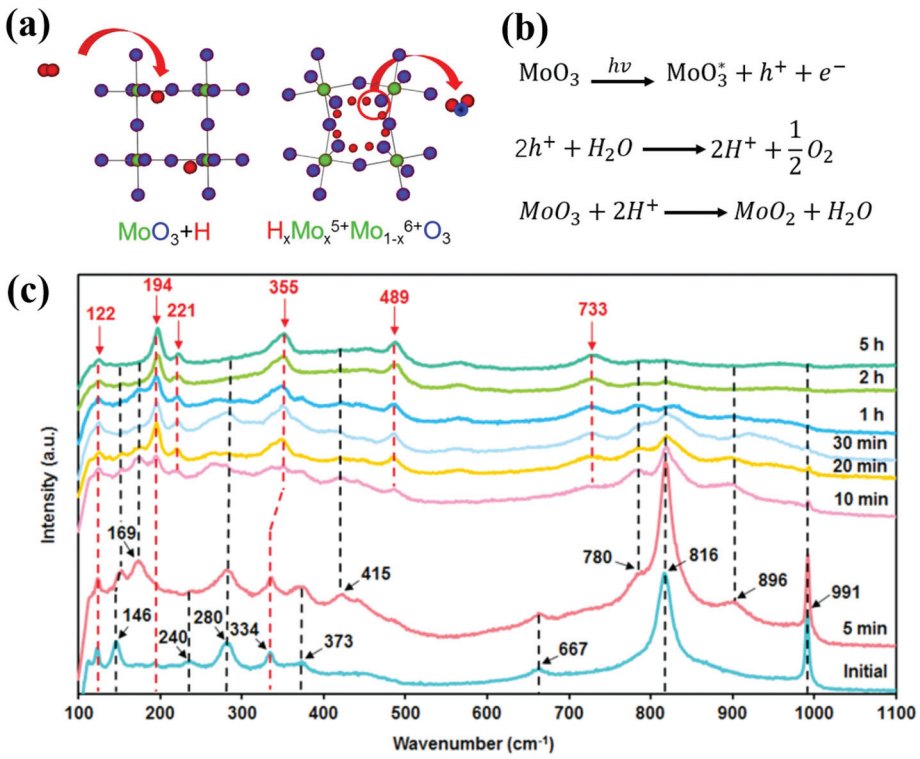

Fig. 13 (a) Schematic illustration of the H intercalation in the MoO_3, and then the H_2O molecule dissociating from the crystal in the MoO_3.[95] Reproduced with permission. Copyright 2017, The Springer Nature Publishing Group. (b) The photocatalytic process of the MoO_3 solution under light irradiation. Adapted from ref. 160. (c) The evolution of the 2D MoO_{3-x} nanoflakes when exposed to the simulated solar light for different times.[160] Reproduced with permission. Copyright 2014, Wiley-VCH.

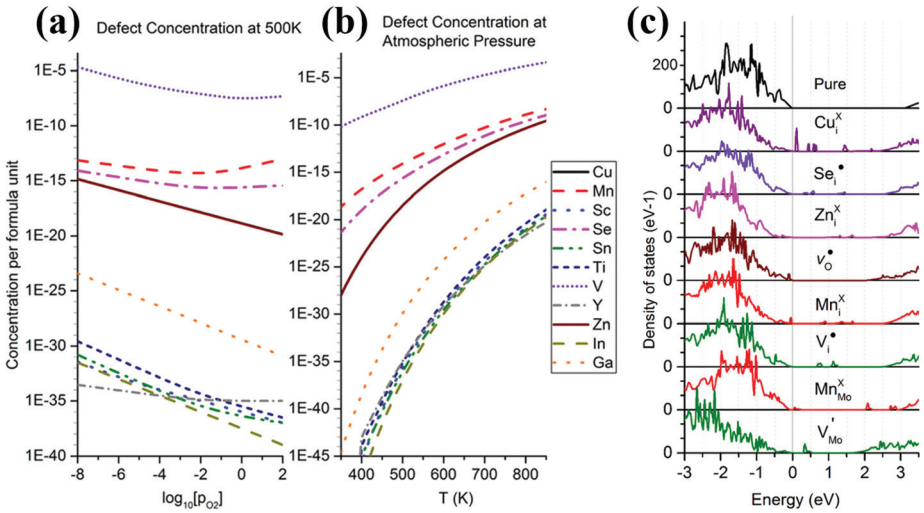

Fig. 14 (a) The equilibrium solubility curve for the elements at a temperature of 500 K with varied O_2 partial pressure. (b) Atmospheric pressure with varied temperature. (c) The electronic density of states introduced by varied dopants.[143] Reproduced with permission. Copyright 2018, The American Chemical Society.

defect levels near the valence band. On the other hand, Mn and V are found to be highly soluble in the MoO_3, and substitutional or interstitial type defects can be formed in a wide range of doping concentrations. In the meantime, band structure calculation results in Fig. 14c further evidence that the Mn and V atoms (Mn_i or V_i) in the interstitial position tend to introduce mid-gap states in the MoO_3 crystal, whereas a substitutional Mn (Mn_{Mo}) induces extra defect levels near the conduction band. In contrast, defect levels originating from the substitutional V are closer to the valence band.[143]

Additionally, Sn^{2+} ions are implemented as the dopant to tune the MoO_3 material properties, and either interstitial or substitutional defects are created, introducing wide-distributed defect levels in the band gap. Experimentally, the layered α-MoO_3 nanosheets were prepared by the PVD method. And in order to achieve the Sn^{2+} intercalation, α-MoO_3 was dipped into a beaker with deionized water solution containing 10 mM $SnCl_2$ and 100 mM tartaric acid, then the mixed solution was heated at 60 °C for more than 15 minutes, and thereafter the MoO_3–Sn samples were rinsed with acetone and deionized water to get rid of other impurities absorbed on the surface of the sample (Fig. 15a and b). UV-vis spectra shown in Fig. 15c first reveal that the absorption intensity is enhanced significantly in a broad wavelength range from 300 to 15 000 nm, which is ascribed to charge transfer from Sn^{2+} ions to the Mo^{6+} ions. Thereafter, XPS measurement is further implemented to investigate the atomic details of the material properties. It shows that, after the introduction of Sn^{2+} ions into the MoO_3, both Mo 3d 5/2 and 3d 3/2 peaks are split into doublets, arising from the presence of Mo +5 and +6 oxidation states. And in the meantime, it also indicates that Sn^{2+} ions are oxidized into Sn^{4+} ions, confirming that the electrons are transferred from the Sn^{2+} ions to the Mo^{6+} ions (Fig. 15d).[144]

Other than that, Nb or Ti doping *via* spray pyrolysis in the MoO_x also shows profound influence on the optical and electronic properties of MoO_3.[145,146] It manifests that the dopants induce extra defect levels near the conduction band of the MoO_3, promoting electron intervalence transfer between Mo and dopants. Besides, the above doping process also works for the other metal doping in the MoO_3. For example, it has been confirmed that elements such as Li, Na, K, Nb, W, Fe, Cd, Ce and Eu ions generate additional energy levels in the band gap, reducing the intrinsically wide band gap of MoO_3.[147–153] However, In-doped MoO_3 is found to be transformed into a p-type semiconductor with an increased band gap of ~3.8 eV.[154] This phenomenon also is found in the Ru-doped MoO_3, which is considered to be caused by induced structural defects during the doping process.[155]

Furthermore, H^+ ions are also extensively used as a dopant to engineer the MoO_3 material property. Due to its tiny atom size and single valence electron, introducing H^+ ions into the crystal structure only induces insignificant structural expansion in the MoO_3 with a relatively low migration barrier, and plenty of research studies have been performed to study the intercalation of hydrogen in the MoO_3 as the dopant.[156–158] Usually, the method of preparing hydrogen molybdenum bronze (H_xMoO_3) is *via* the chemical reaction in acid aqueous solution.[136,140,159] It shows that the H^+ ions prefer to attach to the O and form hydroxyl-like radicals, introducing intrinsic defects and contributing excessive electrons to the material. More specifically, based on the intercalated H^+ ion concentration (the concentration is still low if compared to that in the oxygen vacancy formation), three thermodynamically stable phases of H_xMoO_3 can be determined, which are shown in Fig. 16a, including type 1 ($0.23 < x < 0.40$), type 2 ($0.85 < x < 1.04$) and type 3 ($1.55 < x < 1.72$). In type 1 H_xMoO_3, the intercalated H^+ ions are relatively low, and therefore the H_xMoO_3

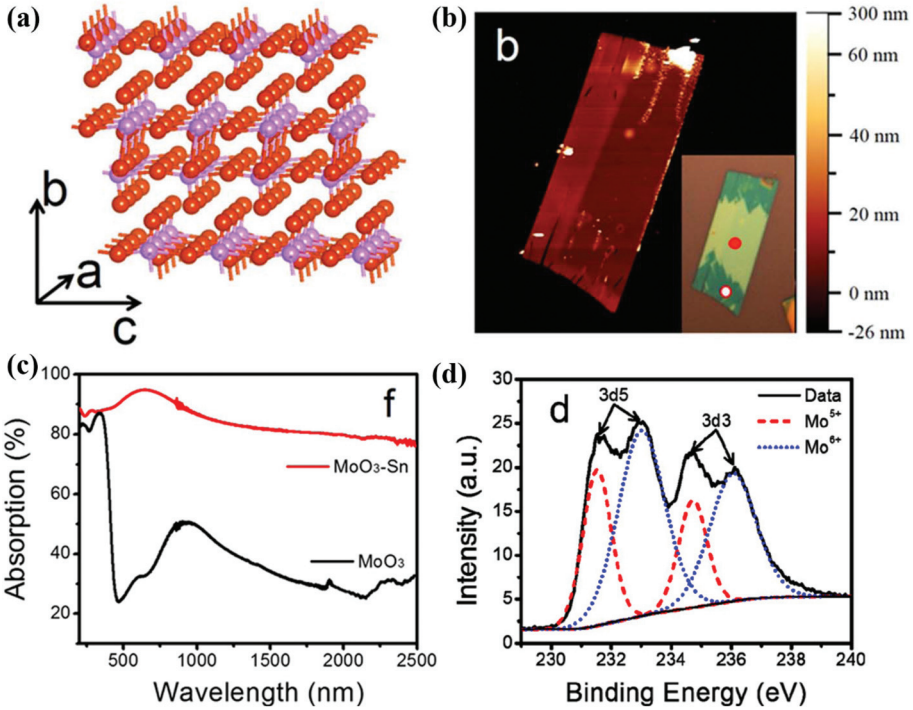

Fig. 15 (a) Atomic structure of the α-MoO_3. (b) The AFM image of the Sn-doped α-MoO_3. (c) The absorption spectra of for the α-MoO_3 and Sn-doped α-MoO_3. (d) The Mo 3d XPS spectra obtained on Sn-doped α-MoO_3.[144] Reproduced with permission. Copyright 2019, The American Chemical Society.

remains in the orthorhombic crystal phase, showing blue colour. However, with the increase of the intercalated H^+ ion amounts, it forms type 2 or type 3 H_xMoO_3, and the crystal phase may evolve from orthorhombic into monoclinic phase, while the colour converts to green (Fig. 16b). In the meantime, XPS valence spectrum analysis shown in Fig. 16c indicates that the valence band edge is determined to be ~3 eV away from the Fermi level for MoO_3; however, weak humps are also detected for the $H_{0.3}MoO_3$, $H_{0.91}MoO_3$ and $H_{1.55}MoO_3$ between the valence band edge and the Fermi level. Physically, these peaks are ascribed to the overlap of the electron wave function induced by free electrons from the intercalated H^+ ions, further revealing the strong interaction of the H^+ ions with the crystal and ultimately shifting up the Fermi level.

In addition to that, the advantage of strong light-material interaction between the incident light and MoO_3 is exploited to introduce H^+ ions into the MoO_3 as well. MoO_x nanoflakes were first prepared by a liquid exfoliation method, and three kinds of MoO_x nanoflake aqueous suspensions (MoO_x-I, MoO_x-II and MoO_x-III) were obtained from the precursors with different MoO_3 and Mo weight ratios (MoO_3, $4MoO_3:1MoO_2$ and $1MoO_3:4MoO_2$). Then, a solar simulator source was used to irradiate the precursors in the experiment. Experimental results show that the MoO_x aqueous suspension under light irradiation can create rich hydroxyl groups in the MoO_3 through the H^+ intercalation process, inducing the electron transfer from the O to Mo. Subsequently, the terminal oxygen atoms transferred charges to the bonding Mo atoms, resulting in partial reduction of molybdenum ions and shortening of Mo–O bonds, which simultaneously leads to the introduction of the defect levels in the MoO_3 band gap (Fig. 17).[141,160] Besides the spill-over method, electron–proton co-doping strategy and annealing in H_2, are also widely implemented, and they show excellent hydrogen introduction efficiency in the MoO_3, consequently promoting the free carrier concentration significantly.[49,95,161]

Crystal phase control

Molybdenum oxides possess various crystal phases, showing diverse optical and electronic properties; therefore, they could be an attractive approach to manipulate the crystal phase for specific optical applications.[126] In a reported experiment, a novel solvothermal method was implemented to synthesize MoO_x nanomaterials. Specifically, MoS_2 dispersed in ethanol was used as the precursor, and H_2O_2 was used as the oxidant. Through reaction time control, monoclinic MoO_2 (JCPDS No. 32-0671) was achieved in the first-time phase, then with the extension of the reaction time, the non-stoichiometric structure of MoO_{3-x} (Mo_4O_{11}) nanoparticles and the stoichiometric structure of MoO_3 nanoparticles were obtained (Fig. 18a).[162] Physical characterization of XRD and XPS detection indicates that the material properties closely rely on the synthetic condition. It reveals that monoclinic MoO_2 nanoparticles with sufficient oxygen-rich groups have been prepared in the first stage, whereas MoO_{3-x} nanoparticles that contain fewer vacancy defects are obtained in the second stage, and stoichio-

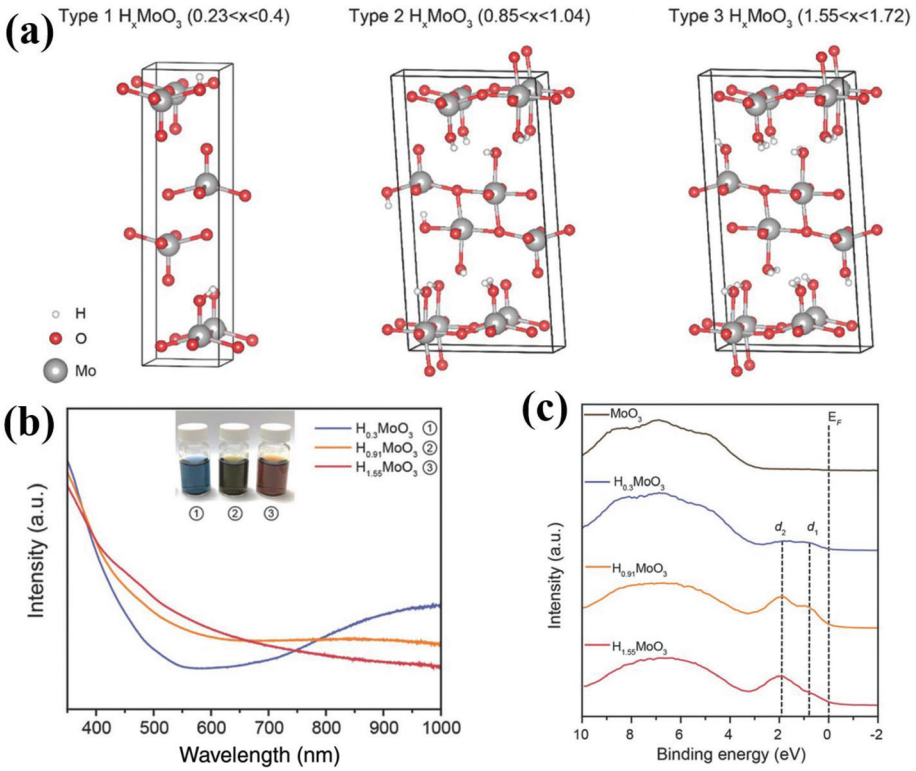

Fig. 16 (a) The atomic structure of the H_xMoO_3 with different H concentrations. (b) The change of the absorption curve of the MoO_3 aqueous solution under light irradiation. (c) The evolution of the 2D MoO_{3-x} nano flake when exposed to the simulated solar light for different times.[140] Reproduced with permission. Copyright 2018, Wiley-VCH.

metric MoO_3 nanoparticles are synthesized in the end. In addition, UV-vis absorption investigation in Fig. 18b illustrates that MoO_2 nanoparticles show intense absorption from visible to NIR with the peak located at 795 nm, which is produced by the strong LSPR effect induced by the d-orbital free electrons from oxygen vacancies. On the other hand, MoO_{3-x} nanoparticles with less defect density show a weaker and narrower absorption profile within the mild visible range, whereas MoO_3 nanoparticles show no absorption from the visible to NIR region, indicating the low free electron density in these two materials. Besides, an alkaline solution (NH^{4+} solution) is also implemented to tune the alkalinity of the electrolysis. By optimizing the doping level of NH^{4+} in the MoO_3 crystal solution, it is shown that highly crystalline orthorhombic 2D molybdenum oxide transits to a hexagonal phase (Fig. 18c).[163]

Other than that, an early study reveals that the amorphous ZnO NC-molecule system is able to promote the interfacial charge-transfer process (ICTP), consequently improving the semiconductor-based SERS performance significantly. Therefore, Li *et al.* presented a quantum size H_xMoO_3 for the similar ICPT property. In a typical experiment, MoS_2 powder was first oxidized in the H_2O_2 solution, and then the mixed solution was quickly transferred into a stainless-steel autoclave with the supercritical CO_2.[164] Through heating it at 40 °C for 3 hours, the CO_2 was released, and the supernatant of MoO_3 quantum dots was collected for the further experiment. Thereafter, the illumination process was conducted with sunlight for 5 hours, and the H^+ ions in the solution intercalated into MoO_3 and formed H_xMoO_3 quantum dots (Fig. 19a). It is shown in Fig. 19b that the prepared H_xMO_3 quantum dots are with an average physical size of 4 nm, and no lattice diffraction fringe is observed. Moreover, the UV-vis spectra in Fig. 19c reveal that the quantum dots show dual optical absorption peaks, which is attributed to the increase of the surface carrier density produced by the quantum size constraint.

MoO_x hybrid formation

Molybdenum oxide can be prepared by various chemical synthesis and physical deposition methods; therefore, it enables the researchers to integrate appropriate preparation processes to obtain MoO_x hybrids, pursuing enhanced optical functions. In the most recent research work, Li *et al.* prepared molybdenum tungsten oxide hybrids (MWO) with a strong plasmonic resonance property.[165] Tungsten oxides (WO_x) are transition oxide materials, and widely used for electrochromic glass, photocatalysis and sensing application. It is shows in the literature that rich substoichiometric compositions of WO_x with tunable LSPR properties can be obtained by various types of defect engineering approaches. Thus, in order to reinforce the plasmonic vibration of both WO_x and MoO_x, MWO hybrids are synthesized by using the one-pot solvothermal solution method. The prepared hybrids are in black-blue colour due to

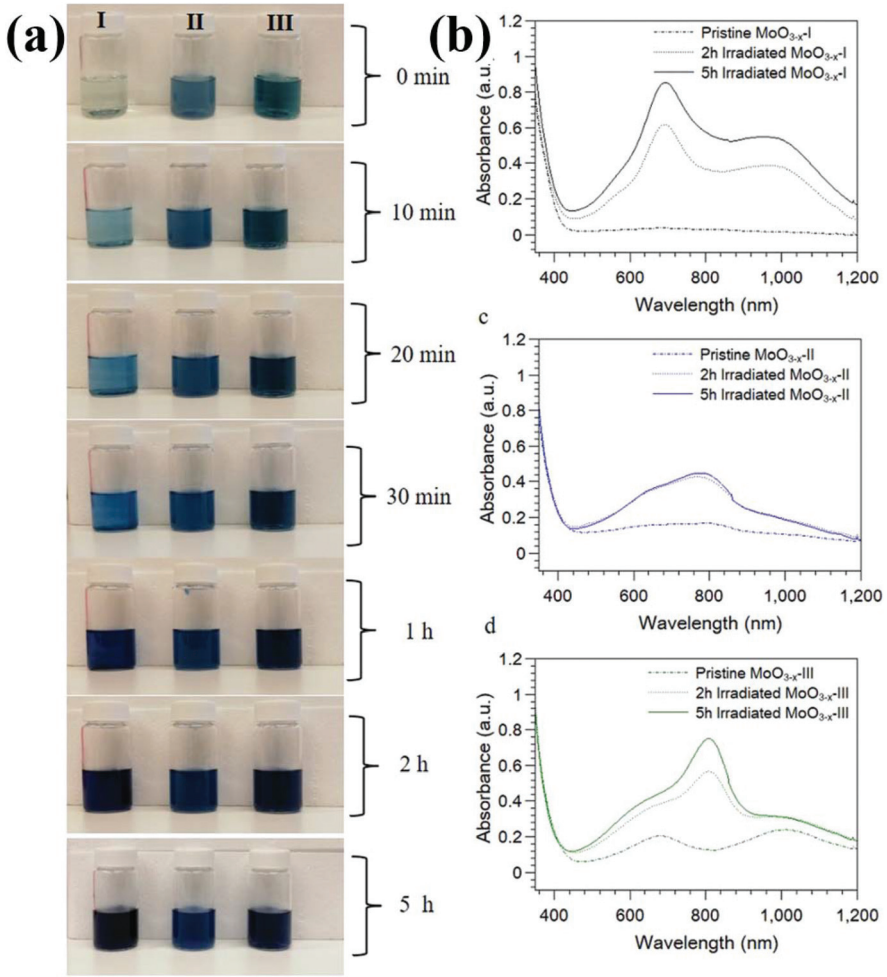

Fig. 17 (a) Photograph of the temporal color change for the MoO_{3-x}-I, MoO_{3-x}-II and MoO_{3-x}-III solution under the light illumination. (b) UV-vis-NIR spectra of the MoO_{3-x}-I, MoO_{3-x}-II and MoO_{3-x}-III solution under the light illumination.[141] Reproduced with permission. Copyright 2019, Wiley-VCH.

the high density of oxygen vacancies, which are reduced by the 2-propanol during the reaction. In the meantime, the Mo and W ions also tend to enter into each other's octahedral structures, creating extra defects in the MWO (Fig. 20a). UV-vis absorption spectra are collected, and they show a broad and strong LSPR effect >400 nm (Fig. 20b), deriving from the high concentration of free electrons. In addition to that, Mo/MoO_2 and MoS_2/MoO_x hybrids are prepared, and experimental characterization shows that hybridizing two materials significantly promotes the free electron density and consequently enhances the SPR intensity.[166,167] In the meantime, MoO_2/graphene oxide hybrids (MoO_2/GO) are also reported in the publication. The hydrothermal reaction is implemented to synthesize the hybrids by Chen *et al.*, and it is shown in Fig. 20c that MoO_2 nanoparticles are completely covered by the ultrathin GO.[168] UV-vis absorption spectra are recorded and show broad absorption peaks centred at 650 nm, revealing the strong LSPR resonance produced by the MoO_2 nanoparticles. Moreover, rich absorption peaks from FTIR spectra further suggest the presence of the abundance of carboxyl and hydroxyl groups on the surface of GO. Therefore, the construction of the above MoO_2/GO hybrids not only retains the LSPR property of MoO_2 nanoparticles, and also raises the absorption density of target probe molecules by the GO coverage. Besides, Achadu *et al.* also prepared Fe_3O_4 functionalized MoO3 nanocubes as the nanotags and graphene as the substrate. By exploiting the plasmonic property of the MoO_3 nanocubes, a reliable hybrid biosensing system based on the immunoassay protocol is constructed for virus detection.[169]

Furthermore, MoO_x and noble metal hybrids (MoO_x/Au, MoO_x/Ag) are reported by researchers for the purpose of utilizing the merits of noble metals and oxide in SERS detection.[170–172] In Guo *et al.* research work, they took advantage of the low valence state of the Mo ions, chloroauric acid ($HAuCl_4$) was directly added into the MoO_x solution, and MoO_x–Au hybrids were synthesized by heating the mixture at 100 °C for 2 minutes. SEM investigation in Fig. 20d confirms the formation of the MoO_x/Au hybrids. In the meantime, the UV-vis absorption spectra also show dual absorption peaks that are derived from LSPR resonance of the Au nanoparticle and MoO_x nanoparticles, which strengthens the SPR intensity as well as expands the LSPR frequency band. In the meantime,

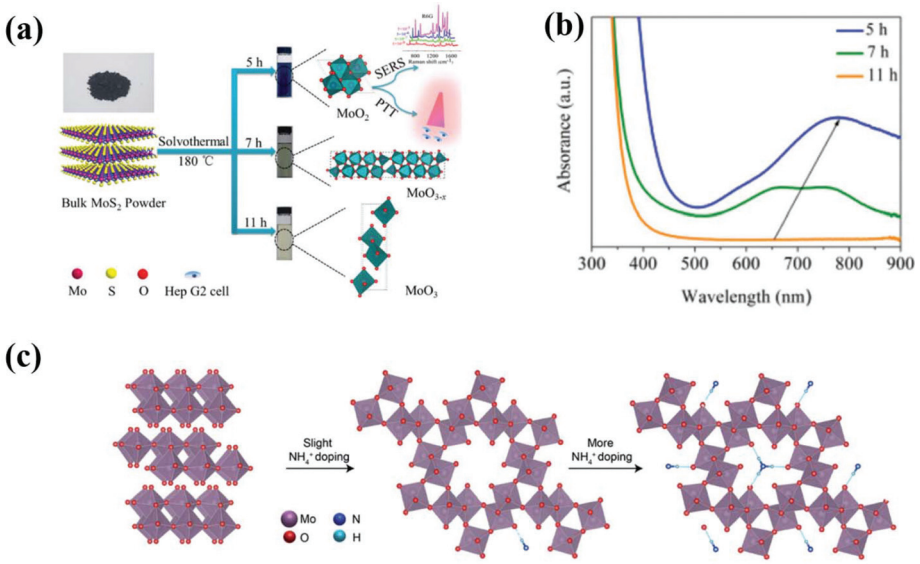

Fig. 18 (a) Schematic illustration of the synthesis method for the MoO_x with different phases. (b) The UV-vis absorption spectra of the MoO_x with different phases. (c) Schematics of the atomic structure evolution with the extending of the reaction time in the NH^{4+} solution.[162] Reproduced with permission. Copyright 2018, Royal Society of Chemistry.

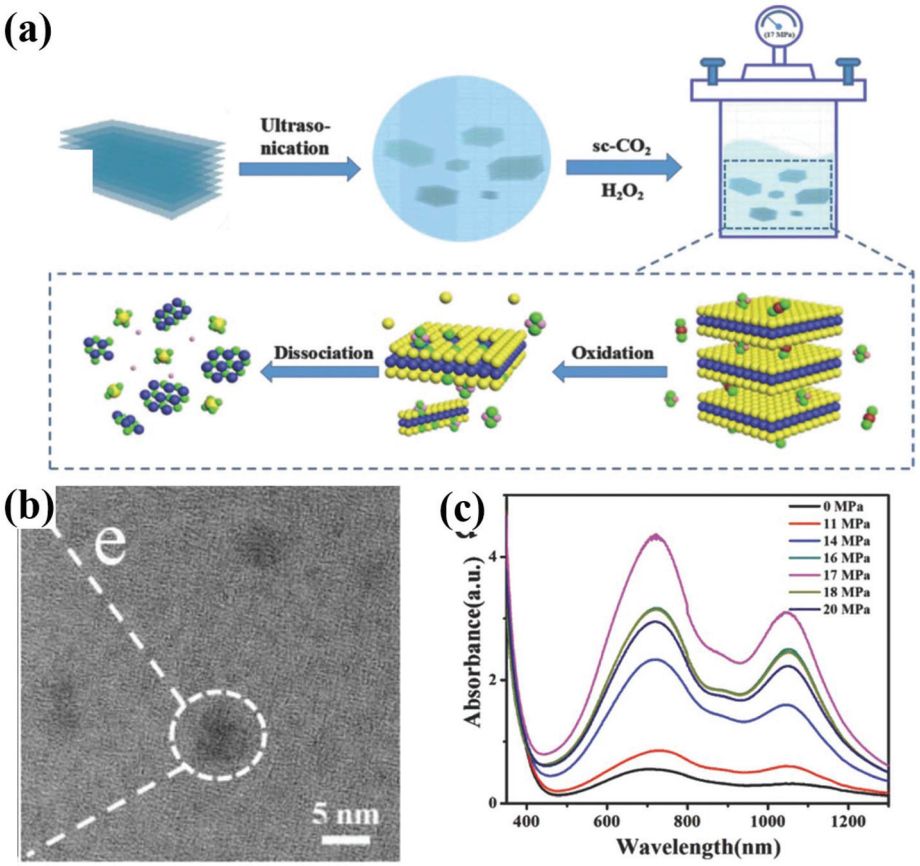

Fig. 19 (a) Schematic illustration of the synthesis process with the supercritical CO_2. (b) The TEM image of the paraded H_xMoO_3 quantum dot. (c) Schematics of the crystal structures evolution with the extending of the reaction time in the NH^{4+} solution.[164] Reproduced with permission. Copyright 2018, Wiley-VCH.

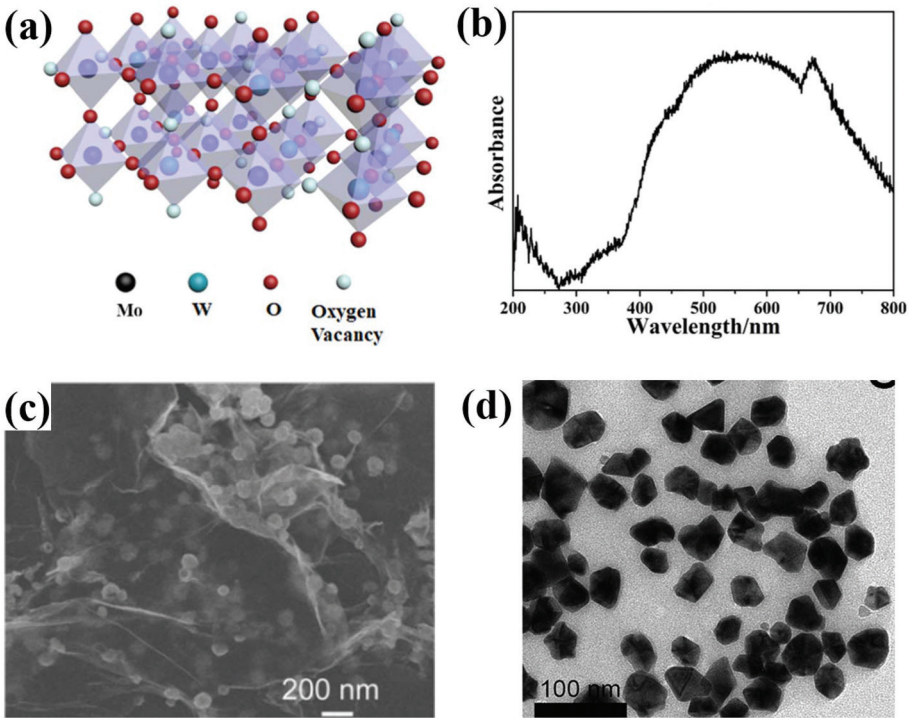

Fig. 20 (a) The atomic structure of the MWO hybrids. (b) The UV-vis absorption spectra of the MWO hybrids. Reproduced with permission.[165] Copyright 2020, The American Chemical Society. (c) The SEM image of the MoO_2/GO hybrids.[168] Reproduced with permission. Copyright 2019, The Springer Nature Publishing Group. (d) The SEM image of the synthesized Au with $HAuCl_4$ as the precursor.[170] Reproduced with permission. Copyright 2019, Elsevier.

similar MoO_x and noble metal hybrids also can be prepared by UV light irradiation or adding a weak reductant in the solution and the same improvement in the SPR intensity is achieved, too.

SERS mechanism and performance of the defective MoO_x

The SERS effect on the surface of the metal oxides was first observed in the 1980s. In the early years, due to the limitations of semiconductor synthesis and characterization technologies, this phenomenon was detected only on several semiconductor surfaces, such as NiO, GaP, and TiO_2, and the Raman enhancement of these semiconductors is found to be relatively weak. Nevertheless, with the progress of the material preparation and tuning technologies, SERS study on the oxide-semiconductor surface has undergone a remarkable growth, especially it is found that the SERS performance of transition metal oxides can be comparable with that of noble metal. However, there are still extensive debates on the SERS mechanisms and SERS performance evaluation; therefore, in the subsequent part of the article, the SERS mechanism and SERS performance of the MoO_x will be reviewed.

SERS mechanism of the defective MoO_x

It is known from theory that Raman signal intensity is closely related to the incident field intensity and polarizability derivative; therefore, two mechanisms for SERS are always discussed, namely electromagnetic enhancement mechanism (EM) and chemical enhancement mechanism (CM).[173] The EM of the SERS involves the electromagnetic field intensity enhancement, which is produced from the surface plasmon resonance excitation. On the other hand, the CM of SERS originates from the molecule polarizability enhancement, which is attributed to the charge transfer between the SERS substrate and molecules.

The plasmon resonance of the material is strongly correlated with the free electron density, and according to the Drude–Lorentz model, it can be estimated as follows:

$$\omega_p = \sqrt{\frac{ne^2}{\varepsilon_0 m_e}}$$

where ω_p is the bulk plasmon resonance frequency.[140] Previously, the surface plasmon resonance excited by the visible light is only found on noble metals. However, the progress in preparing and tuning oxide semiconductors enormously expands the plasmonic material selection. Today, it is shown that a series of substoichiometry oxide-semiconductors also show surface plasmonic resonance that is excited by the visible light range, which is ascribed to the promoted free electron density obtained *via* defect engineering. Especially for the MoO_x, widely tunable localized surface plasmon resonance (LSPR) can be achieved by defect engineering. And plenty of

SERS studies have observed the strong EM that originates from the surficial electromagnetic field generated by the defective MoO_x, which enhances the molecular Raman signal intensity to several orders higher than that on a normal substrate.

On the other hand, theoretical and experimental evidence also reveals that the defective MoO_x possesses rich defect levels in the band gap. Thus, it provides multi-step defect levels to facilitate the charge transfer between the oxide-semiconductor SERS substrate and molecules, and ultimately promotes the molecular polarizability, which is considered as the CM. In a typical experiment, electrons in the ground states gain enough energy by absorbing the incident photon under the specific laser wavelength, and then these excited electrons are transferred to the molecules through the coupled energy level and enhance the polarizability of the molecule, which results in the chemical enhancement of the molecular Raman signal intensity.

Both EM and CM are important for the performance of the MoO_x SERS substrate; however, previous studies indicate that the SERS contributed by EM is always effective when the distance between the substrate and molecules is within the evanescent distance of the surface electromagnetic field, whereas CM only happens when a junction is formed between the substrate and the molecules.

SERS performance of the defective MoO_x

In the early days, the SERS phenomenon exclusively relies on the EM observed on the noble metals; until recently, heavily doped semiconductor materials have been successfully prepared, and they also show prominent EM enhancement. In a reported research study, an 8 nm thick MoO_2 film with a metallic character is prepared by the CVD technique and implemented as the SERS substrate. It is shown in Fig. 21a that the lowest detection concentration of 4×10^{-8} M and enhancement factor of 2.1×10^5 can be obtained, which exceed those of other 2D materials and are comparable to those of noble metal films. Moreover, the Raman signal mapping results also reveal excellent uniformity. It is shown in Fig. 21b that the RSD of Raman peaks in a 5×5 μm^2 area can reach 4.89% (914 cm^{-1}), 5.706% (1182 cm^{-1}), and 5.513% (1622 cm^{-1}), respectively (Fig. 21b). Furthermore, as it can be observed in Fig. 21c, the planar MoO_2 substrate exhibits more environmental stability compared to that of the noble metals, and experimental evidence indicates that even after 15-days in air, the ultra-thin MoO_2 nanosheets still remain nearly the same. In the meantime, the CVD prepared ultrathin film also shows extraordinary temperature stability. It is revealed in Fig. 21d that the shape and SERS performance of the MoO_2

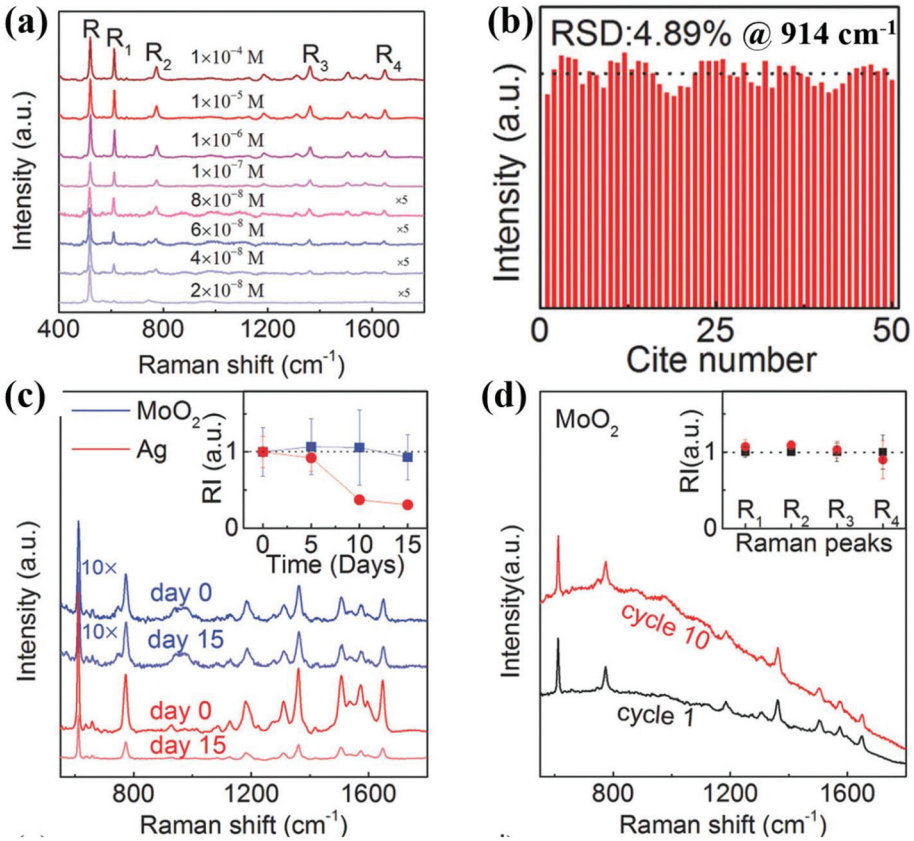

Fig. 21 (a) The Raman spectra measured on the prepared MoO_2 thin film. (b) The statistical distribution of SERS signal intensity (914 cm^{-1}) that was measured on a MoO_2 thin film. (c) Excellent stability of the thin film compared to that of Ag. (d) The reusability of the MoO_2 thin film.[89] Reproduced with permission. Copyright 2018, Wiley-VCH.

nanosheets remain the same when the nanosheets undergo heating treatment at 200 °C for 1 hour. Moreover, Raman measurement demonstrates that the analysts on the surface can be removed by annealing and then the substrate can be reused for more than 10 cycles, showing excellent reusability. In the end, first principles calculation is performed to understand the SERS mechanism of this ultrathin MoO_2. It reveals that MoO_2 presents a metallic character and significant absorption band at 510 nm, both of which can be attributed to the SPR effect (EM) induced by the free electrons, and consequently promotes the SERS performance.[89]

Additionally, the plasmonic properties of the MoO_x are also impacted by their surface states and microstructure. In the experiment, a one-pot and facile solvothermal method by adjusting the synthesis time to prepare different phases of MoO_x nanomaterials is implemented. Practically, MoO_2 (5 hours), MoO_{3-x} (7 hours) and MoO_3 (11 hours) phases of nanoparticles are synthesized by oxidizing the bulk MoS_2 powder through reaction time control. Meanwhile, UV-vis absorption spectra obtained from the three different phase nanoparticles illustrate that MoO_2 nanoparticles display strong SPR absorption in the visible and NIR region, however, MoO_{3-x} nanoparticles show a much weaker LSPR effect, and no LSPR effect is observed for the MoO_3 nanoparticles. The SERS activity is evaluated on the above three different phase nanoparticles. Fig. 22a shows that MoO_2 nanoparticles exhibit a superior SERS effect to that of the MoO_{3-x} and MoO_3 nanoparticles, which is ascribed to the strong LSPR induced by the high oxide vacancy density in the material with shorter reaction time and consequently promotes the EM. Furthermore, SERS performance of the plasmonic MoO_2 nanoparticle substrate is evaluated by probing the molecules of R6G with different concentrations. It can be observed in Fig. 22b and c that the minimum detection concentration of 5×10^{-8} M and the maximum EF up to 1.10×10^7 can be achieved, which even reaches that of noble metals.[162]

Other than the EM mechanism, CM is widely exploited to achieve attractive SERS performance. Research work performed by Ma *et al.* used light to engineer the defect density of the MoO_{3-x}. In the first place, MoO_{3-x} nanosheets are prepared at room temperature by oxidizing the molybdenum powder with H_2O_2, and subsequently the prepared molybdenum oxides are irradiated by the light in methanol to induce the reduction. Physical detection and optical detection are performed. It confirms that MoO_{3-x} nanosheets are in amorphous state. In the meantime, UV-vis absorption spectra in Fig. 23a further reveal that amorphous MoO_{3-x} nanosheets display a strong and wide absorption band from 700 to 1200 nm, which is ascribed to the high-level electron doping from the oxygen vacancies generated during the Xe irradiation phase. SERS performance is evaluated by using a variety of molecules, *e.g.*, MB, RhB and PNTP. As shown in Fig. 23b, it demonstrates that the substrate prepared by amorphous MoO_{3-x} sheets shows more efficient charge transfer capability compared to that of crystal MoO_{3-x}, and using R6G as the Raman reporter (Fig. 23c), it can be observed that attractive SERS performance induced by the CM can be obtained for the amorphous MoO_{3-x} nanosheets under 532 nm laser irradiation, which also exhibits higher sensitivity than the crystalline MoO_{3-x}. Moreover, in Fig. 23d, the recycling detection of the amorphous MoO_{3-x} nanosheets is investigated by repeated oxygen insertion in the H_2O_2 solution and extraction through light-irradiation reduction in methanol. Compared to the crystalline MoO_{3-x}, SERS activity of the a-MoO_{3-x} sheets remains stable upon 5 cycles. This unique SERS property allows the recycling use of the substrate through the H_2O_2-based Fenton-like reaction.[174]

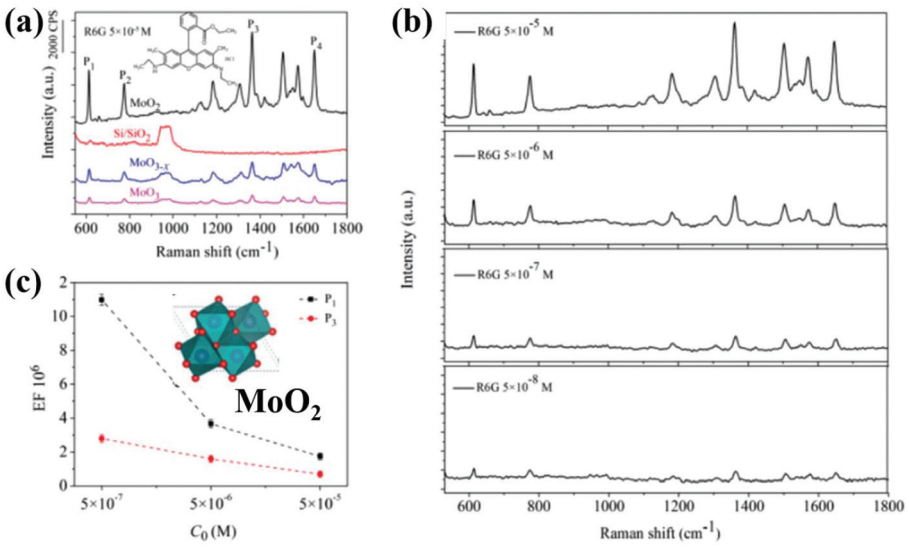

Fig. 22 (a) Raman Spectra of R6G solution (5×10^{-5} M) mixed with MoO_2, MoO_{3-x} and MoO_3 NPS and bare silicon slice. (b) Raman spectra of R6G with different concentration solutions mixed with MoO_2 NPS. (c) The EFs calculated under different R6G concentrations.[162] Reproduced with permission. Copyright 2018, Royal Society of Chemistry.

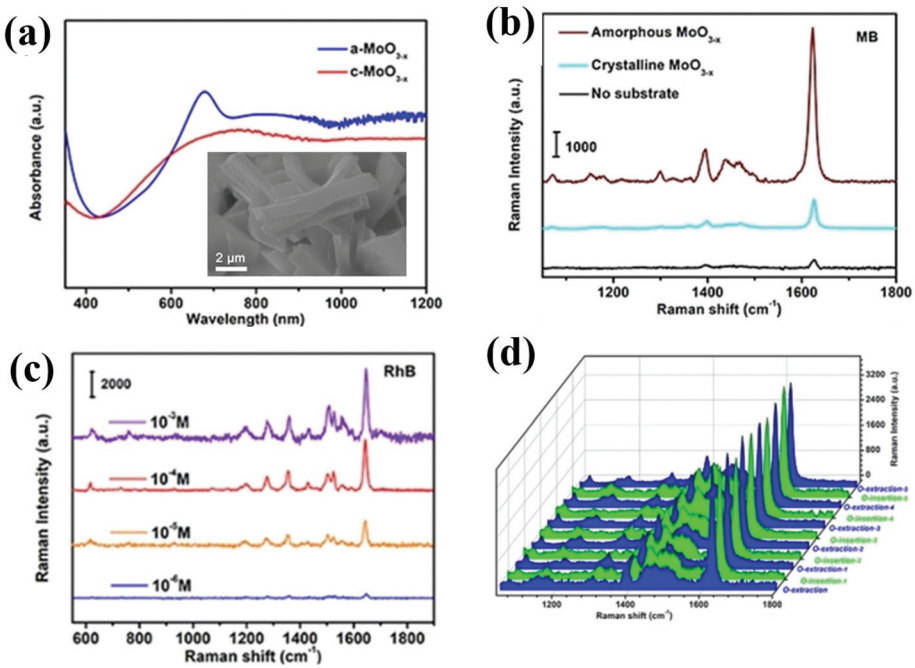

Fig. 23 (a) The UV-vis absorption spectra of the a-MoO_{3-x} and c-MoO_{3-x}. (b) The comparison of SERS spectra collected on the a-MoO_{3-x} and c-MoO_{3-x}. (c) SERS spectra of RhB collected on the a-MoO_{3-x} substrate. (d) The SERS activity of the a-MoO_{3-x} after five cycles of oxygen insertion and extraction experiment.[174] Reproduced with permission. Copyright 2020, European Chemical Societies Publishing.

The plasmonic characteristics of the MoO_x determine the SERS performance, and preparation of tunable and stable plasmonic MoO_x attracts a lot of interest. Therefore, using polydopamine (PDA) as the surface coating, MoO_x nanosheets with the LSPR from the ultraviolet to the near-infrared region (361–809 nm) are prepared through changing the pH value of the reaction solution (Fig. 9b).[131] SERS performance is compared between the blue (lower free electron density) and yellow MoO_{3-x} nanosheets (higher free electron density, Fig. 24a). Using the 532 nm laser as the excitation source, it is illustrated in Fig. 24b that the blue MoO_{3-x} nanosheets achieve a limit of detection of 0.3 fM when rhodamine 6G (R6G) is used as the dye, and the corresponding Raman enhancement factor is calculated to be 1×10^{10}. On the other hand, the yellow MoO_{3-x} nanosheets show much insignificant Raman signal enhancement (Fig. 24c). In view of the experiment evidence, the SERS mechanism of the above MoO_{3-x} nanosheets is discussed. Firstly, it manifests that the Raman signal enhancement of the MoO_{3-x} nanosheets contributed by the LSPR is insignificant, which can be ascribed to the weak surface electromagnetic field induced by the LSPR at both resonance frequencies. However, at this stage, it is observed on the SERS spectra of R6G that the vibrational modes at 612 cm^{-1} and 773 cm^{-1} are highly promoted, which suggests the critical role of CM. Therefore, in the next investigation, the energy band is calculated, and it is revealed that the valence band (VB) and conduction band (CB) are well-aligned with the HOMO and LUMO of the R6G, and consequently triggers charge transfer resonances between the nanosheets and R6G, inducing the remarkable Raman signal improvement (Fig. 24d). Moreover, PDA-coated MoO_{3-x} further shows strong resistance to high concentration of oxidant, such as H_2O_2 and NaClO, it demonstrates that the optical dispersion of the material can remain the same, showing excellent stability for harsh environmental detection application.[133]

Other than that, MoS_{2-x}–MoO_x complex materials also exhibit encouraging SERS capability. Zheng *et al.* reported a kind of MoS_{2-x}–MoO_x mixed phase material prepared through oxygen incorporation into MoS_2 (Fig. 25a and b), and SERS measurement reveals that the substrate prepared by the MoS_{2-x}–MoO_x mixed phase material can have 10 000 times SERS intensity improvement compared to that of the pristine MoS_2 (Fig. 25c). Additionally, annealing treatment of the MoS_{2-x}–MoO_x mixed phase at 300 °C for 40 min brings extra oxygen in the material, and gives 100 000 times higher SERS intensity when referring to the pristine MoS_2 (Fig. 25c). Mechanism investigation is then conducted, as shown in Fig. 25d, oxygen incorporation in the MoS_2 creates additional energy levels, which promotes the charge transfer between the semiconductor and analyte molecule. Besides, it also points out that the improvement of exciton resonances on the semiconductor and molecule produces stronger intensity, which further boosts the charge-transfer resonance in the semiconductor-molecule system.[166]

Furthermore, for a typical MoO_x based SERS substrate, it is observed that both the EM and CM contribute to the SERS enhancement significantly. For instance, a kind of monoclinic-phase MoO_2 nano-dumbbell was prepared by a hydrothermal

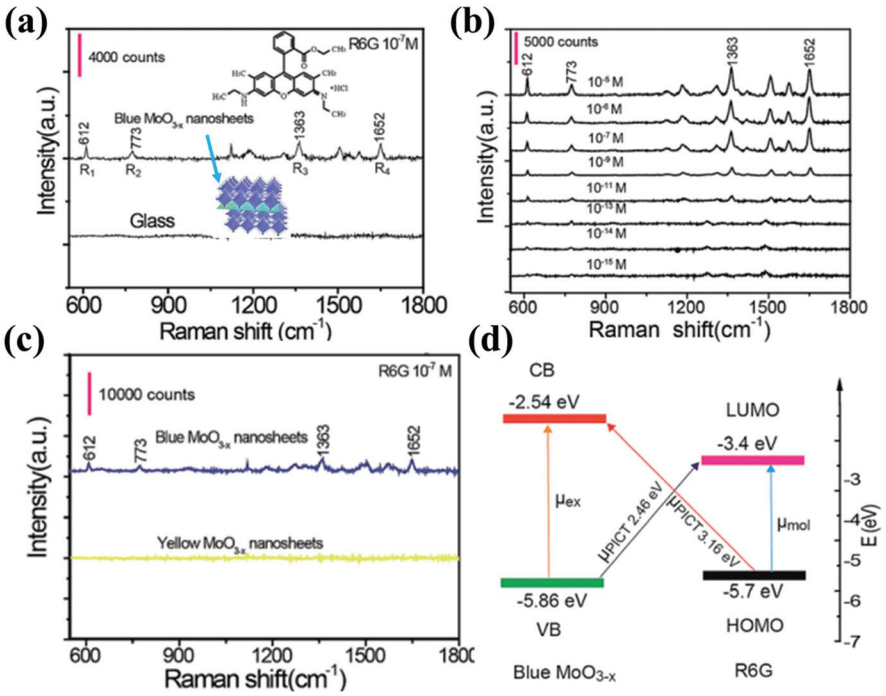

Fig. 24 (a) The SERS spectrum collected on the blue MoO_{3-x} nanosheets when R6G was used as the Raman reporter. (b) The SERS spectra of R6G with different concentrations collected on the blue MoO_{3-x} nanosheets. (c) Comparison of the SERS performance between the blue and yellow MoO_{3-x} nanosheets. (d) The illustration of the photoinduced charge transfer path based on the defect energy level.[133] Reproduced with permission. Copyright 2019, Royal Society of Chemistry.

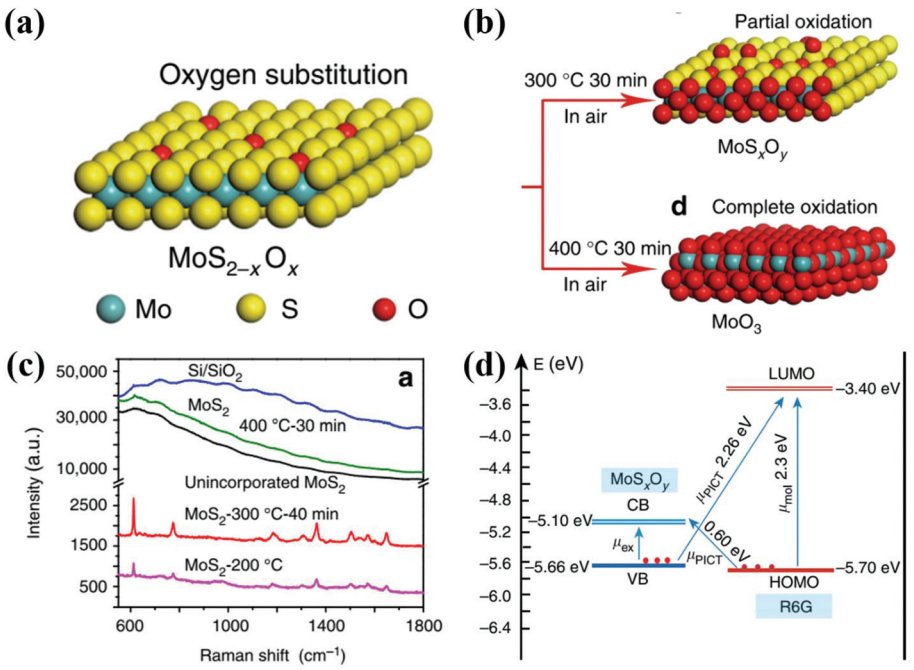

Fig. 25 (a) Atomic illustration of the preparation of $MoS_{2-x}O_x$ through the hydrothermal method. (b) Annealing of $MoS_{2-x}O_x$ sample in the air through different conditions. (c) The SERS spectra measured on respective substrates when R6G is used as the Raman reporter. (d) The charge transfer path for the Raman signal enhancement during the measurement.[166] Reproduced with permission. Copyright 2017, Springer Nature Publishing Group.

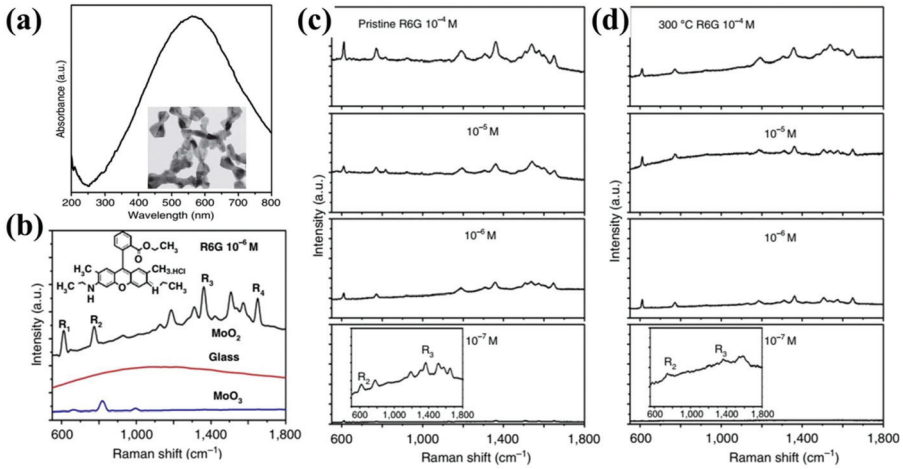

Fig. 26 (a) The TEM image of the hydrothermal prepared MoO_2 nano dumbbells. (b) The SERS spectra measured on the MoO_2 nano when R6G was used as the Raman reporter. (c) The SERS spectra recorded from R6G aqueous solution from 10^{-4} to 10^{-7} M. (d) The SERS spectra collected on the MoO_2 nano dumbbells after 300 °C annealing in the air. The inset in (a) shows the SEM images of the MoO_x nano-dumbbell.[175] Reproduced with permission. Copyright 2017, Springer Nature Publishing Group.

method (Fig. 26a). First principles calculation reveals the metallic characteristics of the MoO_2. In the meantime, UV-vis absorption spectra in Fig. 26a also show strong and well-defined SPR peaks, which are attributed to the high concentration of free electrons in the MoO_2. The SERS performance is then evaluated by using R6G as the Raman reporter (Fig. 26b), it is shown in Fig. 26c that the MoO_2 substrate has an EF of 3.75×10^6 and a high detection sensitivity of 10^{-7} M. Besides, the MoO_2 nano-dumbbell also shows extremely stability under the harsh environment. It is illustrated in Fig. 26d that the

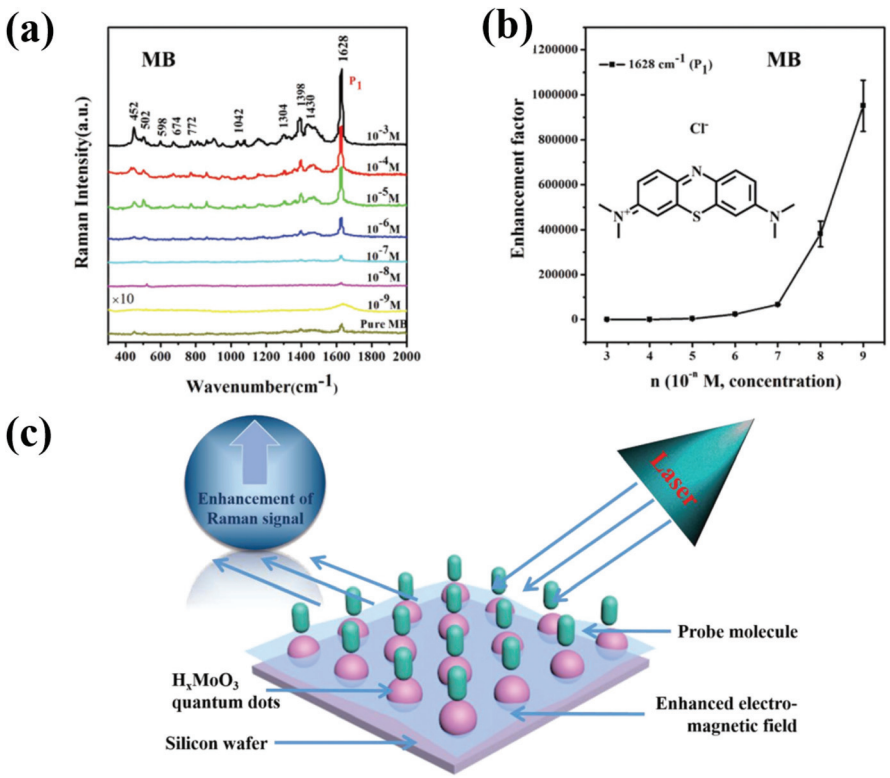

Fig. 27 (a) Raman spectra measured on the H_xMoO_3 quantum dots as the substrate, the H_xMoO_3 quantum were prepared under 15% H_2O_2 and 17 MPa SCO_2. (b) The EF evolution under different MB concentrations. (c) Schematic illustration of the SERS enhancement mechanism by using the H_xMoO_3 quantum dots as the substrate.[164] Reproduced with permission. Copyright 2018, Wiley-VCH.

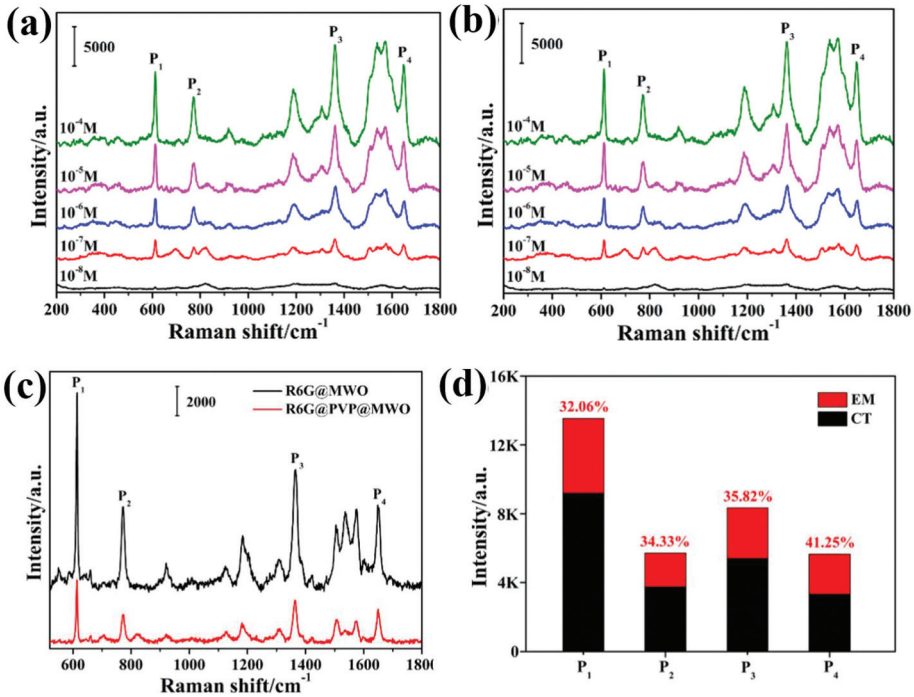

Fig. 28 (a) The SERS spectra of R6G measured on MWO hybrids, commercial WO_3 and commercial MoO_3. (b) The detection limit of the MWO hybrids. (c) SERS spectra of R6G measured on pure MWO hybrids and PVP-coated MWO hybrids. (d) The calculated contributions of EM and CT to SERS.[165] Reproduced with permission. Copyright 2020, The American Chemical Society.

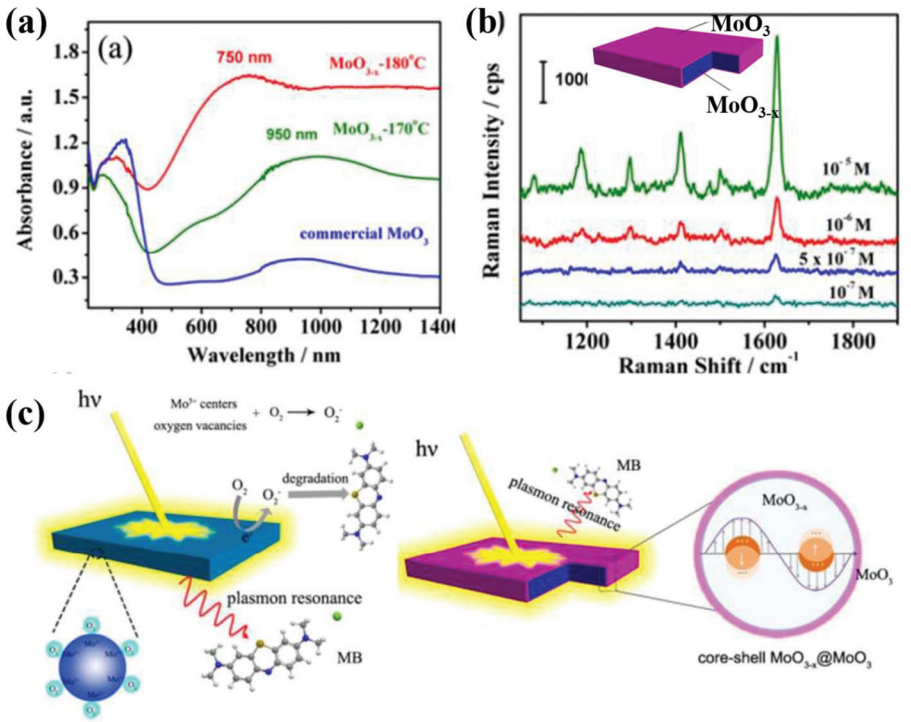

Fig. 29 (a) UV-vis spectra of the MoO_{3-x} nanosheets prepared under different annealing conditions. (b) The SERS spectra measured on MoO_{3-x} nanosheets after annealing at 200 °C for 6 hours. (c) The understanding of the SERS improvement mechanism for the MoO_{3-x} nanosheets after the annealing process.[176] Reproduced with permission. Copyright 2016, Royal Society of Chemistry.

absorption curve of the MoO_2 substrate can sustain even after 300 °C annealing in air. In the end, the SERS enhancement mechanism is discussed. Other than the EM effect, it reveals from the absorption spectra of the R6G-modified MoO_2 substrates that new absorption bands at 349, 485, 536, 580 and 732 nm appear, indicating the coexistence of the charge transfer (CM) between the substrate and molecules.[175]

In addition, amorphous H_xMoO_3 quantum dots possess rich surface defects, and the plasmonic property investigation manifests that they appear dual and strong SPR peaks at 720 and 1050 nm, which can be attributed to the high free electron density from the defects that are confined in a quantum sized dot. The SERS performance of the amorphous H_xMoO_3 quantum dots is evaluated by using MB as the Raman reporter. It shows that the ultrahigh EF of 9.5×10^5 and limit of detection to 10^{-9} M can be obtained on amorphous H_xMoO_3 quantum dots when MB is used as the Raman reporter (Fig. 27a and b). Such a remarkable SERS performance is also shown when R6G and RhB are used as the Raman reporter, which suggests that the amorphous H_xMoO_3 quantum dots not only generate intensive surface electromagnetic field, but also promote the charge transfer, and thus show extremely low trace molecule detection capability. In the meantime, the mechanism of the exceptional SERS property of the H_xMoO_3 quantum dots is discussed; it indicates that the small size of H_xMoO_3 quantum dots can benefit the absorption process of azo dyes, and consequently enhance the interaction between them (Fig. 27c).[164]

Additionally, MoO_x can be prepared by various chemical and physical deposition methods; thus, researchers have integrated suitable preparation methods to obtain MoO_x hybrids, pursuing prominent SERS performance by taking advantage of individual components. In Li *et al.* research work, they prepared molybdenum tungsten oxide hybrids (MWO) for the purpose of integrating the excellent SERS performance of tungsten oxide and molybdenum oxide. Firstly, as illustrated in Fig. 20b, the measured UV-vis absorption spectra show a high and broad absorption peak centred at 552 nm that is ascribed to the high concentration of free electrons produced by the oxygen vacancy defects in the MWO hybrids, and then the SERS performance is measured by using the R6G as the prober molecules. Clearly, it can be observed in Fig. 28a that the SERS signal obtained on R6G@MWO is greatly improved, and the EF of the MWO can reach 10^7 with a detection limit of 10^{-8} M (Fig. 28b). Moreover, the enhancement mechanism of the MWO is discussed, since both tungsten oxides and molybdenum oxides possess the EM and CM characteristics; therefore, a thin PVP layer is coated on the MWO to block the

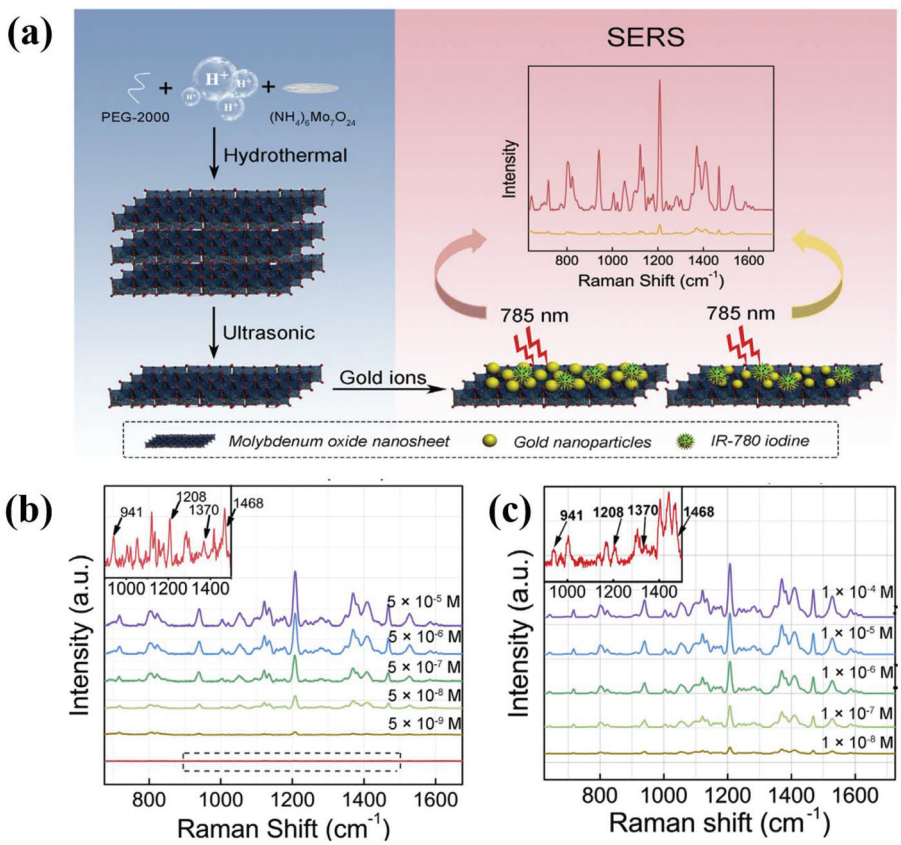

Fig. 30 (a) Schematic illustration of the steps for fabricating the MoO_x-AuNS complex. (b) The SERS spectra of IR-70 obtained in the aqueous solution with MoO_x-AuNSs. (c) The SERS spectra of IR-70 obtained in albumin solution with MoO_x-AuNSs.[170] Reproduced with permission. Copyright 2019, Elsevier.

charge transfer between substrate and molecule, and the SERS spectra are measured again. It is shown obviously in Fig. 28c that the signal is severely reduced when only the EM contributes to the enhancement. And through the calculation, it reveals in Fig. 28d that, due to the high oxygen vacancy defect density, the CM generates more than 50% of the SERS signal enhancement, while the EM from the MWO hybrids contributes the rest enhancement.[165]

To further optimize the CM of the MoO_{3-x}, in the research work presented by Tan *et al.*, shell-isolated MoO_{3-x}@MoO_3 hybrids were prepared by a solvothermal procedure and then annealing treatment at 200 °C in air to form the MoO_3 shell. The plasmonic properties of different MoO_{3-x} nanosheets are evaluated in Fig. 29a; it demonstrates that MoO_{3-x} nanosheets prepared under different annealing conditions show respective SPR frequencies and intensities. Higher temperature at 180 °C generates a broader and stronger absorption peak, indicating much higher free electron concentration in the material. Besides, in the SERS detection of MB with a 785 nm laser, it is observed that the SERS intensity of plasmonic MoO_{3-x} is lower than that observed on the commercial MoO_3, which is ascribed to photocatalytic activity towards the Raman reporter. Nevertheless, the SERS performance investigation of MoO_{3-x}@MoO_3 shown in Fig. 29b reveals a high EF of 1.42×10^5 and an excellent low detection limit of 10^{-7} M. Mechanism analysis indicates that the significant SERS performance improvement of the MoO_{3-x}@MoO_3 is produced by the high free carrier density (5.3×10^{21} cm^{-3}) in the defective bulk MoO_x and prevention of the photocatalytic degradation of the analyte by the non-plasmonic MoO_3 shell (Fig. 29c).[176] In addition, Fe_3O_4 functionalized MoO_3 nanocubes were loaded on the graphene substrate through the immunoassay reaction, and a signal amplification of up to ~10^9-fold was achieved on the above biosensing system, which is ascribed to the combined electromagnetic and chemical mechanisms of the dual SERS nanotag/substrate hybrid system.[169]

On the other hand, ascribed to the reductivity of the low valence Mo ions in MoO_x, the MoO_x also can act as an effective reductant with the help of external stimulation (heating or UV irradiation). Research work presented by Guo *et al.* reported an *in situ* reduction of the Au^{3+} or Ag^+ on the defective MoO_xNSs to prepare molybdenum oxides/noble metal nanoparticles. In the experiment, the defective MoO_x NSs showed excellent reducing ability, and by preparing the mixture with different $HAuCl_4$ volumes, Au nanoparticles (AuNPs) with different sizes scattered on the nanosheets (MoO_x-AuNSs) are prepared (Fig. 30a) under light irradiation. Raman evaluation of the MoO_x-AuNSs reveals that the as-prepared material shows synergistic SERS enhancement produced by both the LSPR enhancement from AuNPs and enrichment of molecules on MoO_x-AuNSs ascribed to electrostatic/hydrophobic interaction. In addition, as shown in Fig. 30b and c, IR-780 iodine is used as the Raman reporter, and the LOD of 5×10^{-9} M and EF of 1.7×10^5 are achieved in aqueous solution. The uniformity of the MoO_x-AuNSs is also investigated, and it shows that the relative standard deviations (RSD) of 11.76% (941 cm^{-1}), 7.37% (1208 cm^{-1}), 6.36% (1370 cm^{-1}) and 4.37% (1468 cm^{-1}) can be achieved. Besides, the merits of the MoO_x/metal hybrids are also reproduced by synthesizing the MoO_x/Ag NPs and MoO_x/Mo hybrids, and relying on the synergetic effect of EM and CM, excellent SERS enhancement as well as uniformity is obtained, too.[170–172]

Challenges and future prospects

We have summarized the recent progress on preparing MoO_x, and two main categories of process techniques, vapor-phase deposition and liquid-phase synthesis, are thoroughly presented. Then, in the second part, the emphasis is put on the review for various material engineering strategies to functionalize the MoO_x. As the compositional and the morphological changes of the MoO_x material critically affect the physical and chemical properties, strategies such as vacancy and dopant introduction, phase control and hybrids formation are presented. Through the review, it is shown that significant progress has been achieved in the controllable preparation and engineering of MoO_x with specific properties and structures, which lay a valuable foundation for MoO_x implemented as the SERS substrate. In the fourth part, the SERS mechanism and various SERS applications based on the MoO_x material are reviewed. Relying on the respective MoO_x material, it shows that the MoO_x with different morphologies, crystal phases and defect densities have either EM/CM or both enhancement mechanisms, and exhibit attractive SERS performance in terms of Raman signal enhancement, large scale uniformity, environment stability and recyclable use.

At this point, it is fair to say that great achievement has been made for the MoO_x used in the SERS application over the past few years; however, further comprehensive investigation on MoO_x is still required. One critical issue can be the catalytic degradation phenomenon. As stated in the review, the SERS on the semiconductor oxides depends on the PICT procedure, and higher defect density usually facilitates the charge transfer between the substrate and molecules, however, it is also observed in the experiment that the Raman dyes tend to be photocatalytically degraded, and high density of defects in the oxides generate more active radicals, which further promotes the photo-catalytic process and degrades the SERS sensitivity. Presently, this photo-catalytic issue has attracted researcher's attention, and some practical solutions have been proposed; however, it is expected that more efforts are still needed to find a better solution. The second obstacle for the MoO_x used as a flexible SERS sensor lies on the facile tuning method of MoO_x material properties. Although a plethora of methods has been developed, it can be found that most of these methods are implemented before the MoO_x are fabricated into SERS sensors. Nevertheless, for an advanced and flexible applicable sensor, it is necessary to have the merit that the SERS performance can be *in situ* tuned, depending on the detection requirement. Currently, some prototypes of light or electric field tuning have been reported, but more studies are still needed

to further build the knowledge on sensor structure design and tuning parameter optimization. The last key issue lies on the enhancement mechanism investigation. Previously, physical theory has comprehensively depicted the surface electromagnetic field property produced by the surface plasmon polaritons on the noble metal, which lays the solid foundation for the EM of the noble metal SERS effect. However, for heavily doped oxide semiconductors, although the carrier concentration can be tuned to 10^{21} cm^{-3} or even higher, the localized characteristics of these electrons from defects are not considered, and thus a further study on the physical model of the surface plasmon polaritons related to the carrier concentration in the oxide semiconductor is needed. In addition, for the noble-metal-based substrates, constructing the "hot spots" is an important approach for further improving the SERS performance; however, this approach is hardly investigated yet. On the other hand, for the CM, it is widely accepted that the charge transfer between the substrate and molecules induces the molecular polarization change, producing an enhanced Raman signal. And the defect levels within the oxides at this procedure significantly facilitate the charge transfer process; however, according to the condensed mater physics, the charge life on different defect levels varies, as a consequence, the charge transfer rate will be affected when the oxide is engineered with diverse defect types that have different defect level properties. Finally, although various defect engineering strategies have been reviewed in the manuscript, alternative material engineering methods like ion implantation, laser irradiation, Ar bombardment and building heterojunction are also encouraged to be further investigated in the future.

In summary, this review has covered the recent achievement in the MoO_x preparing and material property tuning approaches. Then, the SERS mechanism and performance of the various defective MoO_x substrates are thoroughly surveyed, and the SERS enhancement mechanism, performance uniformity, enhancement factor and recyclability of the MoO_x based SERS substrate are evaluated. In all, MoO_x is emerging as a promising candidate for SERS application; however more encouraging research studies are still desirable to build both better knowledge of MoO_x materials and understanding of the chemical enhancement model.

Conflicts of interest

There are no conflicts to declare.

Acknowledgements

This research was funded by the National Natural Science Funding of China (Grant No. 61704095 and 61905161), Natural Science Foundation of Zhejiang Province (Grant No. LY19F050002), the Natural Science Funding of Ningbo (Grant No. 2019A610058) and the K. C. Wong Magna Fund in Ningbo University. This project has also received funding from the European Union's Horizon 2020 Research and Innovation Program under the Marie Sklodowska-Curie grant agreement no. 798916.

Notes and references

1 M. Fleischmann, P. J. Hendra and A. J. McQuillan, *Chem. Phys. Lett.*, 1974, **26**, 163–166.
2 M. G. Albrecht and J. A. Creighton, *J. Am. Chem. Soc.*, 1977, **99**, 5215–5217.
3 D. L. Jeanmaire and R. P. Van Duyne, *J. Electroanal. Chem. Interfacial Electrochem.*, 1977, **84**, 1–20.
4 R. Rani, A. Yoshimura, S. Das, M. R. Sahoo, A. Kundu, K. K. Sahu, V. Meunier, S. K. Nayak, N. Koratkar and K. S. Hazra, *ACS Nano*, 2020, **14**, 6258–6268.
5 J. Langer, D. Jimenez de Aberasturi, J. Aizpurua, R. A. Alvarez-Puebla, B. Auguié, J. J. Baumberg, G. C. Bazan, S. E. J. Bell, A. Boisen, A. G. Brolo, J. Choo, D. Cialla-May, V. Deckert, L. Fabris, K. Faulds, F. J. García de Abajo, R. Goodacre, D. Graham, A. J. Haes, C. L. Haynes, C. Huck, T. Itoh, M. Käll, J. Kneipp, N. A. Kotov, H. Kuang, E. C. Le Ru, H. K. Lee, J.-F. Li, X. Y. Ling, S. A. Maier, T. Mayerhöfer, M. Moskovits, K. Murakoshi, J.-M. Nam, S. Nie, Y. Ozaki, I. Pastoriza-Santos, J. Perez-Juste, J. Popp, A. Pucci, S. Reich, B. Ren, G. C. Schatz, T. Shegai, S. Schlücker, L.-L. Tay, K. G. Thomas, Z.-Q. Tian, R. P. Van Duyne, T. Vo-Dinh, Y. Wang, K. A. Willets, C. Xu, H. Xu, Y. Xu, Y. S. Yamamoto, B. Zhao and L. M. Liz-Marzán, *ACS Nano*, 2020, **14**, 28–117.
6 W. Lv, C. Gu, S. Zeng, J. Han, T. Jiang and J. Zhou, *Biosens. Bioelectron.*, 2018, **8**, 2–10.
7 C.-S. Ho, N. Jean, C. A. Hogan, L. Blackmon, S. S. Jeffrey, M. Holodniy, N. Banaei, A. A. E. Saleh, S. Ermon and J. Dionne, *Nat. Commun.*, 2019, **10**, 4927.
8 E. Mitsai, A. Kuchmizhak, E. Pustovalov, A. Sergeev, A. Mironenko, S. Bratskaya, D. P. Linklater, A. Balčytis, E. Ivanova and S. Juodkazis, *Nanoscale*, 2018, **10**, 9780–9787.
9 J. Yu, Y. Wei, H. Wang, C. Zhang, Y. Wei, M. Wang, B. Man and F. Lei, *Opt. Express*, 2019, **27**, 9879–9894.
10 Z. Huang, A. Zhang, Q. Zhang and D. Cui, *J. Mater. Chem. B*, 2019, **7**, 3755–3774.
11 D. Zhang, L. Huang, B. Liu, H. Ni, L. Sun, E. Su, H. Chen, Z. Gu and X. Zhao, *Biosens. Bioelectron.*, 2018, **106**, 204–211.
12 Y. Chen, H. Liu, Y. Tian, Y. Du, Y. Ma, S. Zeng, C. Gu, T. Jiang and J. Zhou, *ACS Appl. Mater. Interfaces*, 2020, **12**, 14386–14399.
13 Y. Ma, Y. Du, Y. Chen, C. Gu, T. Jiang, G. Wei and J. Zhou, *Chem. Eng. J.*, 2020, **381**, 122710.
14 P. Wang, W. Liu, W. Lin and M. Sun, *J. Raman Spectrosc.*, 2017, **48**, 1144–1147.
15 Y. Du, H. Liu, Y. Chen, Y. Tian, X. Zhang, C. Gu, T. Jiang and J. Zhou, *Appl. Surf. Sci.*, 2020, **528**, 146953.

16 T. Jiang, X. Wang, J. Zhou, D. Chen and Z. Zhao, *Nanoscale*, 2016, **8**, 4908–4914.
17 A. Kundu, R. Rani and K. S. Hazra, *Nanoscale*, 2019, **11**, 16245–16252.
18 Q. Chen, Y. Jia, S. Xie and Z. Xie, *Chem. Soc. Rev.*, 2016, **45**, 3207–3220.
19 J. Reguera, J. Langer, D. Jiménez de Aberasturi and L. M. Liz-Marzán, *Chem. Soc. Rev.*, 2017, **46**, 3866–3885.
20 S. Zhou, M. Zhao, T.-H. Yang and Y. Xia, *Mater. Today*, 2019, **22**, 108–131.
21 J.-F. Li, Y.-J. Zhang, S.-Y. Ding, R. Panneerselvam and Z.-Q. Tian, *Chem. Rev.*, 2017, **117**, 5002–5069.
22 M. I. Halawa, J. Lai and G. Xu, *Mater. Today Nano*, 2018, **3**, 9–27.
23 H. K. Lee, Y. H. Lee, C. S. L. Koh, G. C. Phan-Quang, X. Han, C. L. Lay, H. Y. F. Sim, Y.-C. Kao, Q. An and X. Y. Ling, *Chem. Soc. Rev.*, 2019, **48**, 731–756.
24 J. Dong, X. Zhao, E. Cao, Q. Han, L. Liu, W. Zhang, W. Gao, J. Shi, Z. Zheng, D. Han and M. Sun, *Mater. Today Nano*, 2020, **9**, 100067.
25 T. Jiang, G. Chen, X. Tian, S. Tang, J. Zhou, Y. Feng and H. Chen, *J. Am. Chem. Soc.*, 2018, **140**, 15560–15563.
26 G. Maiorano, L. Rizzello, M. A. Malvindi, S. S. Shankar, L. Martiradonna, A. Falqui, R. Cingolani and P. P. Pompa, *Nanoscale*, 2011, **3**, 2227–2232.
27 S. Zhou, J. Li, K. D. Gilroy, J. Tao, C. Zhu, X. Yang, X. Sun and Y. Xia, *ACS Nano*, 2016, **10**, 9861–9870.
28 X. Zhang, S. Si, X. Zhang, W. Wu, X. Xiao and C. Jiang, *ACS Appl. Mater. Interfaces*, 2017, **9**, 40726–40733.
29 M. Potara, S. Boca, E. Licarete, A. Damert, M.-C. Alupei, M. T. Chiriac, O. Popescu, U. Schmidt and S. Astilean, *Nanoscale*, 2013, **5**, 6013–6022.
30 C. Niu, B. Zou, Y. Wang, L. Cheng, H. Zheng and S. Zhou, *Langmuir*, 2016, **32**, 858–863.
31 J. Choi, Y. Luo, R. B. Wehrspohn, R. Hillebrand, J. Schilling and U. Gösele, *J. Appl. Phys.*, 2003, **94**, 4757–4762.
32 B. Guha, J. Cardenas and M. Lipson, *Opt. Express*, 2013, **21**, 26557–26563.
33 M. Abb, Y. Wang, N. Papasimakis, C. H. de Groot and O. L. Muskens, *Nano Lett.*, 2014, **14**, 346–352.
34 F. Zhou, Z. Zhou, J. Chen, T. H. Choy, J. Wang, N. Zhang, Z. Lin, S. Yu, J. Kang, H. S. P. Wong and Y. Chai, *Nat. Nanotechnol.*, 2019, **14**, 776–782.
35 A. Otto, *J. Raman Spectrosc.*, 2005, **36**, 497–509.
36 H. Ren, S. Sun, J. Cui and X. Li, *Cryst. Growth Des.*, 2018, **18**, 6326–6369.
37 X. Wang and L. Guo, *Angew. Chem.*, 2020, **59**, 4231–4239.
38 S. Cong, Y. Yuan, Z. Chen, J. Hou, M. Yang, Y. Su, Y. Zhang, L. Li, Q. Li, F. Geng and Z. Zhao, *Nat. Commun.*, 2015, **6**, 7800.
39 X. Jiang, K. Song, X. Li, M. Yang, X. Han, L. Yang and B. Zhao, *ChemistrySelect*, 2017, **2**, 3099–3105.
40 J. Lin, Y. Shang, X. Li, J. Yu, X. Wang and L. Guo, *Adv. Mater.*, 2017, **29**, 1604797.
41 T. Yan, L. Zhang, T. Jiang, Z. Bai, X. Yu, P. Dai and M. Wu, *Appl. Surf. Sci.*, 2017, **419**, 373–381.
42 M. Gao, J. Yao, Y. Quan, J. Yang, P. Huo, J. Dai, Y. Yan and C. Ma, *J. Mater. Sci.: Mater. Electron.*, 2019, **30**, 20537–20543.
43 R. Haldavnekar, K. Venkatakrishnan and B. Tan, *Nat. Commun.*, 2018, **9**, 3065.
44 C. Zhou, L. Sun, F. Zhang, C. Gu, S. Zeng, T. Jiang, X. Shen, D. S. Ang and J. Zhou, *ACS Appl. Mater. Interfaces*, 2019, **11**, 34091–34099.
45 Y. Yin, P. Miao, Y. Zhang, J. Han, X. Zhang, Y. Gong, L. Gu, C. Xu, T. Yao, P. Xu, Y. Wang, B. Song and S. Jin, *Adv. Funct. Mater.*, 2017, **27**, 1606694.
46 L. Zhou, J. Zhou, W. Lai, X. Yang, J. Meng, L. Su, C. Gu, T. Jiang, E. Y. B. Pun, L. Shao, L. Petti, X. W. Sun, Z. Jia, Q. Li, J. Han and P. Mormile, *Nat. Commun.*, 2020, **11**, 1785.
47 G. Barbillon, *Nanomaterials*, 2020, **10**, 1200.
48 I. A. de Castro, R. S. Datta, J. Z. Ou, A. Castellanos-Gomez, S. Sriram, T. Daeneke and K. Kalantar-zadeh, *Adv. Mater.*, 2017, **29**, 1701619.
49 H. Cheng, X. Qian, Y. Kuwahara, K. Mori and H. Yamashita, *Adv. Mater.*, 2015, **27**, 4616–4621.
50 H. Li, L. McRae, C. J. Firby, M. Al-Hussein and A. Y. Elezzabi, *Nano Energy*, 2018, **47**, 130–139.
51 Z. Xu, Q. Zhang and W. Zhai, *RSC Adv.*, 2015, **5**, 93554–93562.
52 S. J. Xiao, X. J. Zhao, P. P. Hu, Z. J. Chu, C. Z. Huang and L. Zhang, *ACS Appl. Mater. Interfaces*, 2016, **8**, 8184–8191.
53 M. Hossain, S. Rashkeev, V. Madhavan, T. Zhang, C.-Y. Lee, B. Hoex, N. Tabet and A. Abdallah, Proc. of UPVSEC2018, 2018, 2018-1AO.1.6, 15–19.
54 S. Balendhran, S. Walia, M. Alsaif, E. P. Nguyen, J. Z. Ou, S. Zhuiykov, S. Sriram, M. Bhaskaran and K. Kalantar-zadeh, *ACS Nano*, 2013, **7**, 9753–9760.
55 O. J. Achadu, K. Takemura, I. M. Khoris and E. Y. Park, *Sens. Actuators, B*, 2020, **321**, 128494.
56 B. Dong, Y. Huang, N. Yu, Y. Fang, B. Cao, Y. Li, H. Xu and M. Sun, *Chem. – Asian J.*, 2010, **5**, 1824–1829.
57 Y. Chen, C. Lu, L. Xu, Y. Ma, W. Hou and J.-J. Zhu, *CrystEngComm*, 2010, **12**, 3740–3747.
58 D. D. Yao, J. Z. Ou, K. Latham, S. Zhuiykov, A. P. O'Mullane and K. Kalantar-zadeh, *Cryst. Growth Des.*, 2012, **12**, 1865–1870.
59 Q. Qu, W.-B. Zhang, K. Huang and H.-M. Chen, *Comput. Mater. Sci.*, 2017, **130**, 242–248.
60 A. H. Reshak, *RSC Adv.*, 2015, **5**, 22044–22052.
61 M. P. Mitoraj and A. Michalak, *J. Struct. Chem.*, 2012, **23**, 1369–1375.
62 X. Xiao, C. Zhang, S. Lin, L. Huang, Z. Hu, Y. Cheng, T. Li, W. Qiao, D. Long, Y. Huang, L. Mai, Y. Gogotsi and J. Zhou, *Energy Storage Mater.*, 2015, **1**, 1–8.
63 T. Mizushima, Y. Moriya, N. H. H. Phuc, H. Ohkita and N. Kakuta, *Catal. Commun.*, 2011, **13**, 10–13.
64 N. A. Chernova, M. Roppolo, A. C. Dillon and M. S. Whittingham, *J. Mater. Chem.*, 2009, **19**, 2526–2552.
65 E. M. McCarron and J. C. Calabrese, *J. Solid State Chem.*, 1991, **91**, 121–125.

66 C. V. Ramana, I. B. Troitskaia, V. V. Atuchin, M. Ramos and D. Ferrer, *J. Vac. Sci. Technol.*, 2010, **28**, 726–729.
67 H. Hu, C. Deng, J. Xu, K. Zhang and M. Sun, *J. Exp. Nanosci.*, 2015, **10**, 1336–1346.
68 F. Reale, K. Sharda and C. Mattevi, *Appl. Mater. Today*, 2016, **3**, 11–22.
69 C. Muratore, A. A. Voevodin and N. R. Glavin, *Thin Solid Films*, 2019, **688**, 137500.
70 Z. Wei and S. Zhuiykov, *Nanoscale*, 2019, **11**, 15709–15738.
71 S. Balendhran, S. Walia, H. Nili, J. Z. Ou, S. Zhuiykov, R. B. Kaner, S. Sriram, M. Bhaskaran and K. Kalantar-zadeh, *Adv. Funct. Mater.*, 2013, **23**, 3952–3970.
72 P. Dwivedi, S. Dhanekar and S. Das, *Semicond. Sci. Technol.*, 2016, **31**, 115010.
73 W.-C. Chang, X. Qi, J.-C. Kuo, S.-C. Lee, S.-K. Ng and D. Chen, *CrystEngComm*, 2011, **13**, 5125–5132.
74 D. Ban, N. Xu, S. Deng, J. S. Chen and J. She, *J. Mater. Res. Technol.*, 2010, **26**, 584–588.
75 R. Senthilkumar, G. Anandhababu, T. Mahalingam and G. Ravi, *J. Energy Chem.*, 2016, **25**, 798–804.
76 K. Kalantar-zadeh, J. Tang, M. Wang, K. L. Wang, A. Shailos, K. Galatsis, R. Kojima, V. Strong, A. Lech, W. Wlodarski and R. B. Kaner, *Nanoscale*, 2010, **2**, 429–433.
77 Y. Wang, X. Du, J. Wang, M. Su, X. Wan, H. Meng, W. Xie, J. Xu and P. Liu, *ACS Appl. Mater. Interfaces*, 2017, **9**, 5543–5549.
78 D. Wang, J.-N. Li, Y. Zhou, D.-H. Xu, X. Xiong, R.-W. Peng and M. Wang, *Appl. Phys. Lett.*, 2016, **108**, 053107.
79 M. F. Al-Kuhaili, S. M. A. Durrani and I. A. Bakhtiari, *Appl. Phys. A: Mater. Sci. Process.*, 2009, **98**, 609–615.
80 M. A. Camacho-López, L. Escobar-Alarcón and E. Haro-Poniatowski, *Appl. Phys. A: Mater. Sci. Process.*, 2004, **78**, 59–65.
81 S. Santhosh, M. Mathankumar, S. Selva Chandrasekaran, A. K. Nanda Kumar, P. Murugan and B. Subramanian, *Langmuir*, 2017, **33**, 19–33.
82 T. Aoki, T. Matsushita, K. Mishiro, A. Suzuki and M. Okuda, *Thin Solid Films*, 2008, **517**, 1482–1486.
83 O. M. Hussain, K. Srinivasa Rao, K. V. Madhuri, C. V. Ramana, B. S. Naidu, S. Pai, J. John and R. Pinto, *Appl. Phys. A: Mater. Sci. Process.*, 2002, **75**, 417–422.
84 C. V. Ramana and C. M. Julien, *Chem. Phys. Lett.*, 2006, **428**, 114–118.
85 T. Ivanova, K. Gesheva and A. Szekeres, *J. Solid State Electrochem.*, 2002, **7**, 21–24.
86 J. Wang, I. Matsubara, N. Murayama, S. Woosuck and N. Izu, *Thin Solid Films*, 2006, **514**, 329–333.
87 K. Gesheva, A. Cziraki, T. Ivanova and A. Szekeres, *Thin Solid Films*, 2005, **492**, 322–326.
88 T. Ivanova, K. A. Gesheva, G. Popkirov, M. Ganchev and E. Tzvetkova, *Mater. Sci. Eng., B*, 2005, **119**, 232–239.
89 H. Wu, X. Zhou, J. Li, X. Li, B. Li, W. Fei, J. Zhou, J. Yin and W. Guo, *Small*, 2018, **14**, 1802276.
90 B. B. Wang, X. L. Qu, M. K. Zhu, Y. A. Chen, K. Zheng, X. X. Zhong, U. Cvelbar and K. Ostrikov, *J. Alloys Compd.*, 2018, **765**, 1167–1173.
91 Y. Chen and B. Wang, *Opt. Mater.*, 2019, **92**, 150–155.
92 M. Koyano, S. Ōhara, H. Negishi, M. Sasaki, M. Inoue, M. Nomura and H. Fujiwara, *Phys. Status Solidi B*, 1988, **147**, 559–565.
93 Y. J. Lee, Y. I. Seo, S.-H. Kim, D.-G. Kim and Y. D. Kim, *Appl. Phys. A: Mater. Sci. Process.*, 2009, **97**, 237–241.
94 W. V. Schulmeyer and H. M. Ortner, *Int. J. Refract. Met. Hard Mater.*, 2002, **20**, 261–269.
95 A. Borgschulte, O. Sambalova, R. Delmelle, S. Jenatsch, R. Hany and F. Nüesch, *Sci. Rep.*, 2017, **7**, 40761.
96 O. de Melo, L. García-Pelayo, Y. González, O. Concepción, M. Manso-Silván, R. López-Nebreda, J. L. Pau, J. C. González, A. Climent-Font and V. Torres-Costa, *J. Mater. Chem. C*, 2018, **6**, 6799–6807.
97 A. Chithambararaj, N. Rajeswari Yogamalar and A. C. Bose, *Cryst. Growth Des.*, 2016, **16**, 1984–1995.
98 D. Ding, W. Guo, C. Guo, J. Sun, N. Zheng, F. Wang, M. Yan and S. Liu, *Nanoscale*, 2017, **9**, 2020–2029.
99 J. S. Chen, Y. L. Cheah, S. Madhavi and X. W. Lou, *J. Phys. Chem. C*, 2010, **114**, 8675–8678.
100 L. Fang, Y. Shu, A. Wang and T. Zhang, *J. Phys. Chem. C*, 2007, **111**, 2401–2408.
101 R. Liang, H. Cao and D. Qian, *Chem. Commun.*, 2011, **47**, 10305–10307.
102 S. Hu and X. Wang, *J. Am. Chem. Soc.*, 2008, **130**, 8126–8127.
103 H. Cheng, T. Kamegawa, K. Mori and H. Yamashita, *Angew. Chem., Int. Ed.*, 2014, **53**, 2910–2914.
104 Y. Xu, M. Zhou, X. Wang, C. Wang, L. Liang, F. Grote, M. Wu, Y. Mi and Y. Lei, *Angew. Chem., Int. Ed.*, 2015, **54**, 8768–8771.
105 X. Yu, G. Zhang, Z. Lu, J. Liu, X. Lei and X. Sun, *CrystEngComm*, 2014, **16**, 3935–3939.
106 Y. Jin and P. K. Shen, *J. Mater. Chem. A*, 2015, **3**, 20080–20085.
107 Y. Song, J. Zhao, Y. Zhao, Z. Huang, Y. Li and G. Wu, *CrystEngComm*, 2016, **18**, 6502–6512.
108 Z. Li, J. Ma, B. Zhang, C. Song and D. Wang, *CrystEngComm*, 2017, **19**, 1479–1485.
109 K. Sakaushi, J. Thomas, S. Kaskel and J. Eckert, *Chem. Mater.*, 2013, **25**, 2557–2563.
110 V. V. Kumar, K. Gayathri and S. P. Anthony, *Mater. Res. Bull.*, 2016, **76**, 147–154.
111 P. Jittiarporn, L. Sikong, K. Kooptarnond and W. Taweepreda, *Ceram. Int.*, 2014, **40**, 13487–13495.
112 M. Parashar, V. K. Shukla and R. Singh, *J. Mater. Sci.: Mater. Electron.*, 2020, **31**, 3729–3749.
113 J. X. Tang, C. S. Lee and S. T. Lee, *J. Appl. Phys.*, 2007, **101**, 064504.
114 S. Cong, T. Sugahara, T. Wei, J. Jiu, Y. Hirose, S. Nagao and K. Suganuma, *Cryst. Growth Des.*, 2015, **15**, 4536–4542.
115 T. Brezesinski, J. Wang, S. H. Tolbert and B. Dunn, *Nat. Mater.*, 2010, **9**, 146–151.
116 H. Yin, Y. Kuwahara, K. Mori, H. Cheng, M. Wen and H. Yamashita, *J. Mater. Chem. A*, 2017, **5**, 8946–8953.

117 S. Koçak, F. N. Ertaş and Z. Dursun, *Appl. Surf. Sci.*, 2013, **265**, 205–213.
118 A. Quintana, A. Varea, M. Guerrero, S. Suriñach, M. D. Baró, J. Sort and E. Pellicer, *Electrochim. Acta*, 2015, **173**, 705–714.
119 D. D. Yao, M. R. Field, A. P. O'Mullane, K. Kalantar-Zadeh and J. Z. Ou, *Nanoscale*, 2013, **5**, 10353–10359.
120 G. Zhao, L. Zhang and K. Sun, *J. Electroanal. Chem.*, 2013, **694**, 61–67.
121 E. Gómez, E. Pellicer and E. Vallés, *J. Electroanal. Chem.*, 2005, **580**, 238–244.
122 D. Sinkeviciute, J. Baltrusaitis and N. Dukstiene, *J. Solid State Electrochem.*, 2010, **15**, 711–723.
123 R. S. Patil, M. D. Uplane and P. S. Patil, *Appl. Surf. Sci.*, 2006, **252**, 8050–8056.
124 S. N. Lou, N. Yap, J. Scott, R. Amal and Y. H. Ng, *Sci. Rep.*, 2014, **4**, 7428.
125 M. Szkoda, K. Trzciński, K. Siuzdak and A. Lisowska-Oleksiak, *Electrochim. Acta*, 2017, **228**, 139–145.
126 K. Inzani, M. Nematollahi, F. Vullum-Bruer, T. Grande, T. W. Reenaas and S. M. Selbach, *Phys. Chem. Chem. Phys.*, 2017, **19**, 9232–9245.
127 H. Peelaers, M. L. Chabinyc and C. G. Van de Walle, *Chem. Mater.*, 2017, **29**, 2563–2567.
128 F. Li and Z. Chen, *Nanoscale*, 2013, **5**, 5321–5333.
129 H.-S. Kim, J. B. Cook, H. Lin, J. S. Ko, S. H. Tolbert, V. Ozolins and B. Dunn, *Nat. Mater.*, 2017, **16**, 454–460.
130 M. Vasilopoulou, A. M. Douvas, D. G. Georgiadou, L. C. Palilis, S. Kennou, L. Sygellou, A. Soultati, I. Kostis, G. Papadimitropoulos, D. Davazoglou and P. Argitis, *J. Am. Chem. Soc.*, 2012, **134**, 16178–16187.
131 M. T. Greiner, L. Chai, M. G. Helander, W.-M. Tang and Z.-H. Lu, *Adv. Funct. Mater.*, 2012, **22**, 4557–4568.
132 G. Song, J. Shen, F. Jiang, R. Hu, W. Li, L. An, R. Zou, Z. Chen, Z. Qin and J. Hu, *ACS Appl. Mater. Interfaces*, 2014, **6**, 3915–3922.
133 J. Wang, Y. Yang, H. Li, J. Gao, P. He, L. Bian, F. Dong and Y. He, *Chem. Sci.*, 2019, **10**, 6330–6335.
134 Y. Li, J. Cheng, Y. Liu, P. Liu, W. Cao, T. He, R. Chen and Z. Tang, *J. Mater. Chem. C*, 2017, **121**, 5208–5214.
135 R. Li, H. An, W. Huang and Y. He, *Sens. Actuators, B*, 2018, **259**, 59–63.
136 W. Zhang, H. Li, C. J. Firby, M. Al-Hussein and A. Y. Elezzabi, *ACS Appl. Mater. Interfaces*, 2019, **11**, 20378–20385.
137 K. Khojier, H. Savaloni and S. Zolghadr, *Appl. Surf. Sci.*, 2014, **320**, 315–321.
138 S. Kasani, P. Zheng, J. Bright and N. Wu, *ACS Appl. Mater. Interfaces*, 2019, **1**, 2389–2395.
139 L. Li, T. Zhang, J. Yan, X. Cai and S. F. Liu, *Small*, 2017, **13**, 1700441.
140 B. Y. Zhang, A. Zavabeti, A. F. Chrimes, F. Haque, L. A. O'Dell, H. Khan, N. Syed, R. Datta, Y. Wang, A. S. R. Chesman, T. Daeneke, K. Kalantar-zadeh and J. Z. Ou, *Adv. Funct. Mater.*, 2018, **28**, 1706006.
141 A. S. Etman, L. Wang, K. Edström, L. Nyholm and J. Sun, *Adv. Funct. Mater.*, 2019, **29**, 1806699.
142 M. M. Y. A. Alsaif, A. F. Chrimes, T. Daeneke, S. Balendhran, D. O. Bellisario, Y. Son, M. R. Field, W. Zhang, H. Nili, E. P. Nguyen, K. Latham, J. van Embden, M. S. Strano, J. Z. Ou and K. Kalantar-zadeh, *Adv. Funct. Mater.*, 2016, **26**, 91–100.
143 D. S. Lambert, A. Lennon and P. A. Burr, *J. Mater. Chem. C*, 2018, **122**, 27241–27249.
144 R. He, Z. Chen, H. Lai, T. Zhang, J. Wen, H. Chen, F. Xie, S. Yue, P. Liu, J. Chen, W. Xie, X. Wang and J. Xu, *ACS Appl. Mater. Interfaces*, 2019, **11**, 15741–15747.
145 S. S. Mahajan, S. H. Mujawar, P. S. Shinde, A. I. Inamdar and P. S. Patil, *Sol. Energy Mater. Sol. Cells*, 2009, **93**, 183–187.
146 N. Usha, R. Sivakumar and C. Sanjeeviraja, *Mater. Lett.*, 2018, **229**, 189–192.
147 H. Li, J. Chen, M. Cui, G. Cai, A. L.-S. Eh, P. S. Lee, H. Wang, Q. Zhang and Y. Li, *J. Mater. Chem. C*, 2016, **4**, 33–38.
148 C. M. Cholant, T. M. Westphal, R. D. C. Balboni, E. A. Moura, A. Gündel, W. H. Flores, A. Pawlicka and C. O. Avellaneda, *J. Solid State Electrochem.*, 2017, **21**, 1509–1515.
149 C. C. Chang, P. W. Chi, P. Chandan and C. K. Lin, *Materials*, 2019, **12**, 2475.
150 Q.-Y. Ouyang, L. Li, Q.-S. Wang, Y. Zhang, T.-S. Wang, F.-N. Meng, Y.-J. Chen and P. Gao, *Sens. Actuators, B*, 2012, **169**, 17–25.
151 S. Bai, C. Chen, D. Zhang, R. Luo, D. Li, A. Chen and C.-C. Liu, *Sens. Actuators, B*, 2014, **204**, 754–762.
152 Z. Liu, Y. Jin, F. Teng, X. Hua and M. Chen, *Catal. Commun.*, 2015, **66**, 42–45.
153 A. Phuruangrat, U. Cheed-Im, T. Thongtem and S. Thongtem, *Mater. Lett.*, 2016, **172**, 166–170.
154 H.-Y. Chen, H.-C. Su, C.-H. Chen, K.-L. Liu, C.-M. Tsai, S.-J. Yen and T.-R. Yew, *J. Mater. Chem.*, 2011, **21**, 5745–5752.
155 M. Balaji, J. Chandrasekaran, M. Raja and S. Rajesh, *J. Mater. Sci.: Mater. Electron.*, 2016, **27**, 11646–11658.
156 X. Sha, L. Chen, A. C. Cooper, G. P. Pez and H. Cheng, *J. Mater. Chem. C*, 2009, **113**, 11399–11407.
157 H. Cheng, M. Wen, X. Ma, Y. Kuwahara, K. Mori, Y. Dai, B. Huang and H. Yamashita, *J. Am. Chem. Soc.*, 2016, **138**, 9316–9324.
158 I. Kostis, N. Vourdas, G. Papadimitropoulos, A. Douvas, M. Vasilopoulou, N. Boukos and D. Davazoglou, *J. Phys. Chem. C*, 2013, **117**, 18013–18020.
159 F. Xie, W. C. H. Choy, C. Wang, X. Li, S. Zhang and J. Hou, *Adv. Mater.*, 2013, **25**, 2051–2055.
160 M. M. Y. A. Alsaif, K. Latham, M. R. Field, D. D. Yao, N. V. Medehkar, G. A. Beane, R. B. Kaner, S. P. Russo, J. Z. Ou and K. Kalantar-zadeh, *Adv. Mater.*, 2014, **26**, 3931–3937.
161 Q. Zhu, S. Jiang, K. Ye, W. Hu, J. Zhang, X. Niu, Y. Lin, S. Chen, L. Song, Q. Zhang, J. Jiang and Y. Luo, *Adv. Mater.*, 2020, **32**, 2004059.

162 Y. Zhan, Y. Liu, H. Zu, Y. Guo, S. Wu, H. Yang, Z. Liu, B. Lei, J. Zhuang, X. Zhang, D. Huang and C. Hu, *Nanoscale*, 2018, **10**, 5997–6004.
163 F. Haque, A. Zavabeti, B. Y. Zhang, R. S. Datta, Y. Yin, Z. Yi, Y. Wang, N. Mahmood, N. Pillai, N. Syed, H. Khan, A. Jannat, N. Wang, N. Medhekar, K. Kalantar-zadeh and J. Z. Ou, *J. Mater. Chem. A*, 2019, **7**, 257–268.
164 H. Li, Q. Xu, X. Wang and W. Liu, *Small*, 2018, **14**, 1801523.
165 P. Li, L. Zhu, C. Ma, L. Zhang, L. Guo, Y. Liu, H. Ma and B. Zhao, *ACS Appl. Mater. Interfaces*, 2020, **12**, 19153–19160.
166 Z. Zheng, S. Cong, W. Gong, J. Xuan, G. Li, W. Lu, F. Geng and Z. Zhao, *Nat. Commun.*, 2017, **8**, 1–10.
167 X. Zhou, X. Zhao, F. Xie, Z. Jin, X. Song, W. Xie, X. Wang and Z. Tang, *ACS Appl. Mater. Interfaces*, 2020, **3**, 5656–5664.
168 J. Chen, K. Sun, Y. Zhang, D. Wu, Z. Jin, F. Xie, X. Zhao and X. Wang, *Anal. Bioanal. Chem.*, 2019, **411**, 2781–2791.
169 O. J. Achadu, F. Abe, T. Suzuki and E. Y. Park, *ACS Appl. Mater. Interfaces*, 2020, **12**, 43522–43534.
170 Y. Guo, Z. Zhuang, Z. Liu, W. Fan, H. Zhong, W. Zhang, Y. Ni and Z. Guo, *Appl. Surf. Sci.*, 2019, **480**, 1162–1170.
171 Y. Xu, K. Lai, C. Gu, T. Jiang, X. Shen, S. Zeng, A. H.-P. Ho, D. S. Ang and J. Zhou, *Phys. Status Solidi RRL*, 2020, 2000499.
172 L. Su, Y. Xiong, Z. Chen, Z. Duan, Y. Luo, D. Zhu and X. Ma, *Sens. Actuators, B*, 2019, **279**, 320–326.
173 G. C. Schatz, M. A. Young and R. P. Duyne, in *Surface-Enhanced Raman Scattering-Physics and Applications*, ed. K. Kneipp, M. Moskovits and J. Kneipp, Springer, Berlin, 2006, vol. 103.
174 J. Ma, X. Tan, Y. Ma, X. Yao, J. Zhang and L. Wang, *Chem. – Eur. J.*, 2020, **26**, 2653–2657.
175 Q. Zhang, X. Li, Q. Ma, Q. Zhang, H. Bai, W. Yi, J. Liu, J. Han and G. Xi, *Nat. Commun.*, 2017, **8**, 14903.
176 X. Tan, L. Wang, C. Cheng, X. Yan, B. Shen and J. Zhang, *Chem. Commun.*, 2016, **52**, 2893–2896.